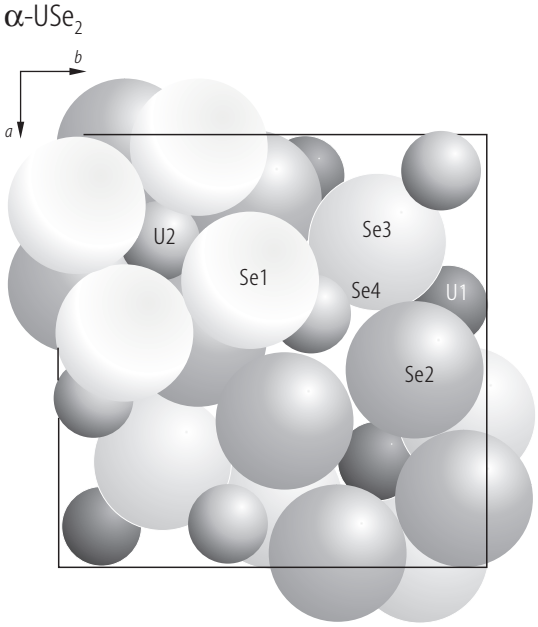

Fig. 380. α-USe_2. Tetragonal crystal structure of SrB_2-type (space group P4/n) projected on the (*ab*)-plane [88BD, 89BD1]. This structure is considered to be a high-temperature form of α-USe_2 being isomorphous with α-US_{2-x} (see Fig. 370). The difference is due to splitting of the 4(c) position in s.g. P4/ncc into two independent 2(c) positions in s.g. P4/n. Here only one of these 2(c) sites is occupied by U2 resulting in a stoichiometric compound. Therefore the quadratic antiprisms are alternatively empty and filled by the U2 atoms.

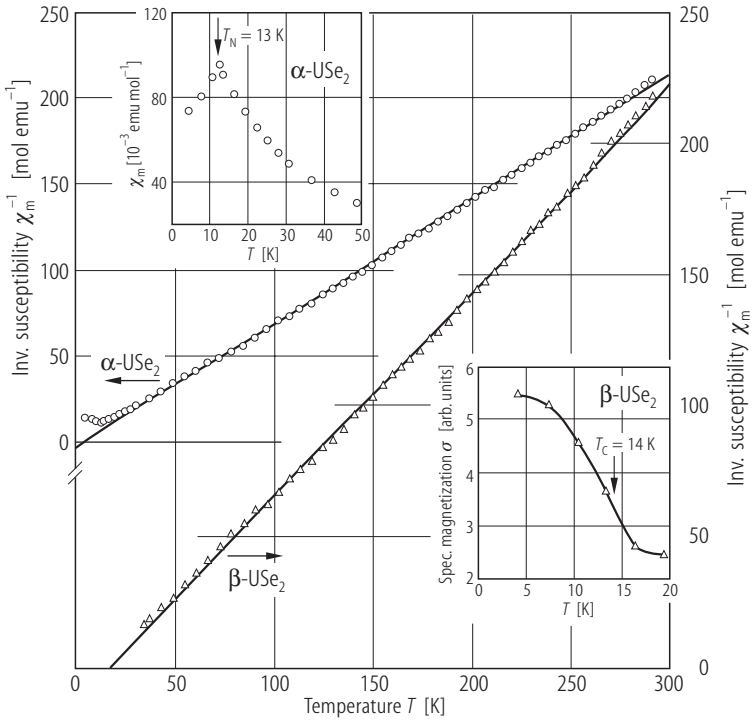

Fig. 381. α-USe_2, β-USe_2. Inverse molar magnetic susceptibility, χ_m^{-1}, vs. temperature, T [95STK]. The solid lines are Curie-Weiss fits with the parameters given in Table F. Upper inset: low temperature magnetic susceptibility vs. T for α-USe_2 (T_N = 13 K); lower inset: thermomagnetic curve for β-USe_2 (T_C = 14 K).

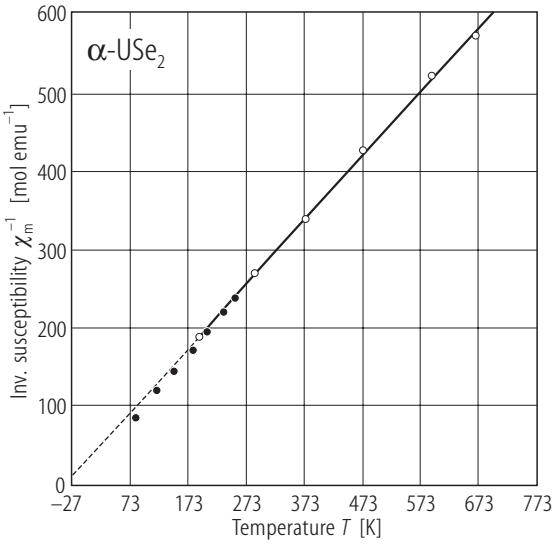

Fig. 382. α-USe_2. Inverse molar magnetic susceptibility, χ_m^{-1}, vs. temperature, T, in the range 80…700 K (open circles) [68GHTT]. For comparison the data reported by [61TS] are shown by full circles. The solid line is a Curie-Weiss fit with $p_{eff} = 3.05\ \mu_B$.

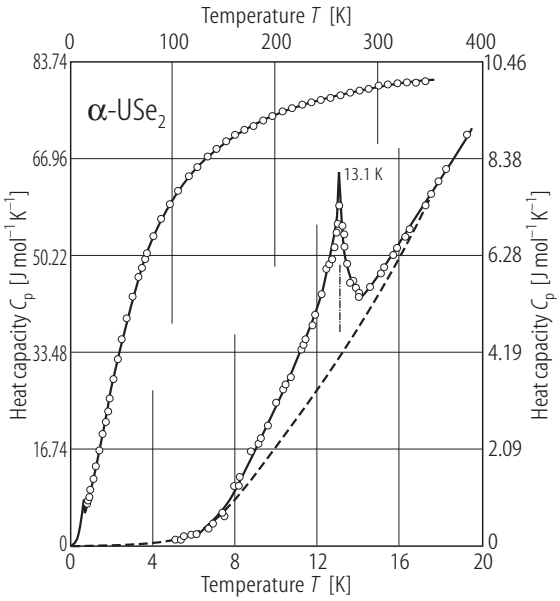

Fig. 383. α-USe_2. Heat capacity, C_p, vs. temperature, T, in the range 20…350 K (upper and left-hand side scale) and 5…20 K (bottom and right-hand side scale) [70WG]. A λ-shaped anomaly at T_N = 13.1 K results from an antiferromagnetic ordering of the uranium magnetic moments. At nearly the same temperature anomalies occur in the magnetic susceptibility (see Fig. 381) and the electrical resistivity (see Fig. 384). The inferred entropy increment 0.80 J/(mol K) is particularly small and therefore it is considered that only a fraction of U atoms is involved in the transition.

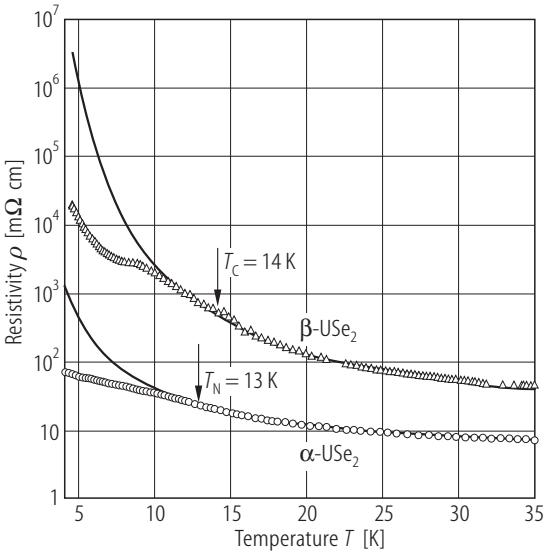

Fig. 384. α-USe_2, β-USe_2, sc. Low temperature electrical resistivity, ρ, vs. temperature, T in the range 4.2…35 K measured with $i \parallel [102]$ and $i \parallel b$ for α- and β-modifications, respectively [95STK]. The solid lines are fits of the experimental data from the range 15…50 K to the equations: $\rho(T)[\text{m}\Omega\text{cm}] = 3.5\exp(4.3\ \text{meV}/2k_BT)$ in the case of α-USe_2 and $\rho(T)[\text{m}\Omega\text{cm}] = 6.6\exp(10.5\ \text{meV}/2k_BT)$ for β-USe_2. Deviations of the experimental curves from these exponential functions are probably due to a gradual closing the semiconducting gap caused by the onset of the ordered states (marked by the arrows).

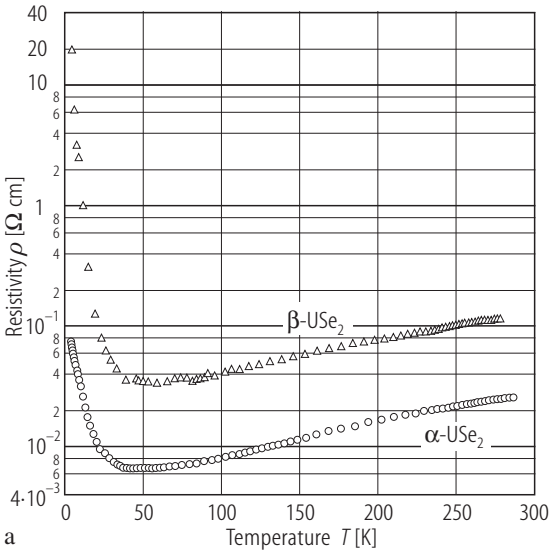

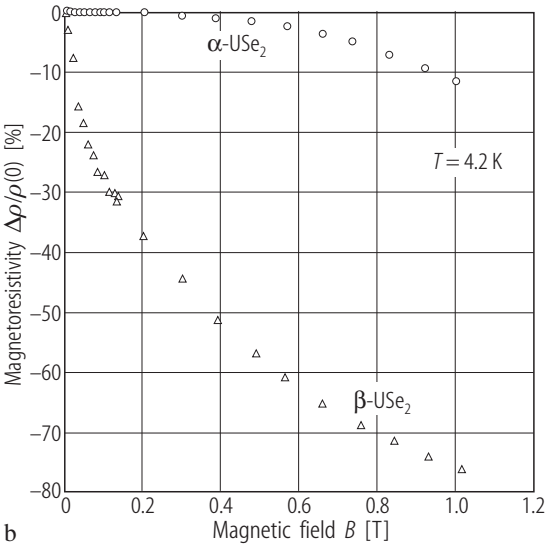

Fig. 385. α-USe_2, β-USe_2, sc. **(a)** Electrical resistivity, ρ, vs. temperature, T, in the range 4.2…300 K, measured with $i \parallel [102]$ and $i \parallel b$ for α- and β-modifications, respectively [95S, 95STK]. **(b)** Transverse magnetoresistivity, $\Delta\rho/\rho(0)$, vs. magnetic field, B, measured at $T = 4.2$ K as in panel **(a)** [95S, 95STK]. The different behavior of the magnetoresistivity is attributed to different magnetic ordering in the two modifications (antiferromagnetic in α-USe_2 and ferromagnetic in β-USe_2). Note that for β-USe_2 a rather weak applied magnetic field brings about a gigantic effect on the electrical resistivity.

For Fig. 387 see next page

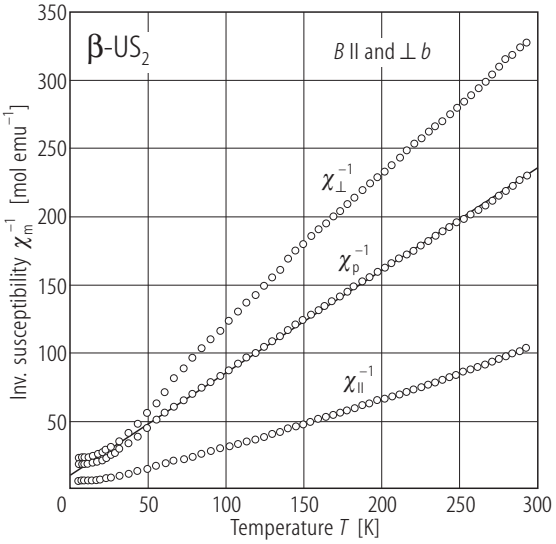

Fig. 386. β-US_2, sc. Inverse molar magnetic susceptibility, χ_m^{-1}, vs. temperature, T, measured with magnetic field applied along and perpendicular to the b-axis [95S, 95STK]. For comparison the powder data, $\chi_p^{-1}(T)$, are also given. The solid line is a Curie-Weiss fit with the parameters given in Table F. All three curves show at low temperatures a Van Vleck behaviour characteristic of a singlet ground state. The observed large anisotropy is due to crystal field interactions.

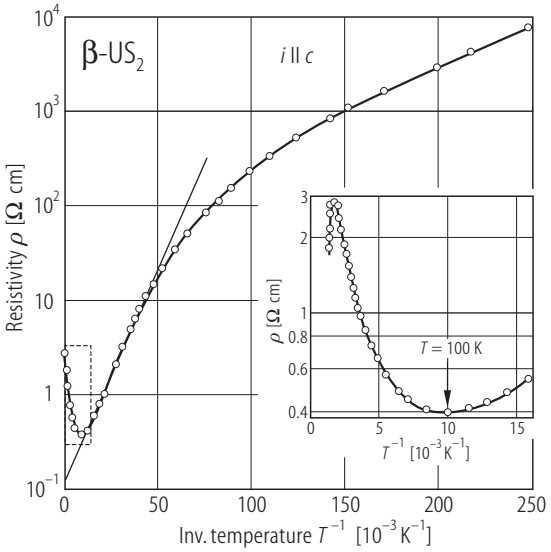

Fig. 388. β-US_2, sc. Electrical resistivity, ρ, vs. inverse temperature, $1/T$, in the range 4.2…650 K, measured with the current flowing along the c-axis [72SGWC]. ρ(300K) = 1 Ωcm; ρ(4.2K) = $7 \cdot 10^3$ Ωcm. Inset: high temperature $\rho(T)$ showing a minimum at 100 K and a maximum at about 600 K. Above the latter temperature the resistivity probably reaches the intrinsic range of semiconductivity with $\Delta E_g = 1.2$ eV. The solid line represents an activation behaviour in the range 20…100 K with $\Delta E_g = 18.6$ meV, which is close to $\Delta E_g = 12.1$ meV reported by [99ST] (compare Fig. 389b).

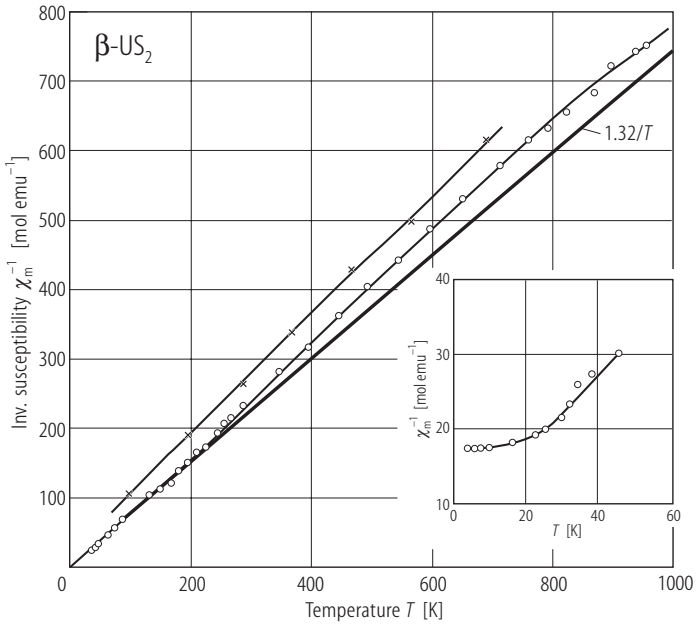

Fig. 387. β-US_2. Inverse molar magnetic susceptibility, χ_m^{-1}, vs. temperature, T, in the range 4.2…1000 K [72SGWC, 73S]. For comparison the results taken from [68GHTT] are shown by crosses. The bold straight line is a Curie law with $p_{eff} = 3.25$ μ_B. Inset: $\chi_m^{-1}(T)$ at low temperatures showing a saturation behaviour characteristic of a nonmagnetic ground state (compare Fig. 386).

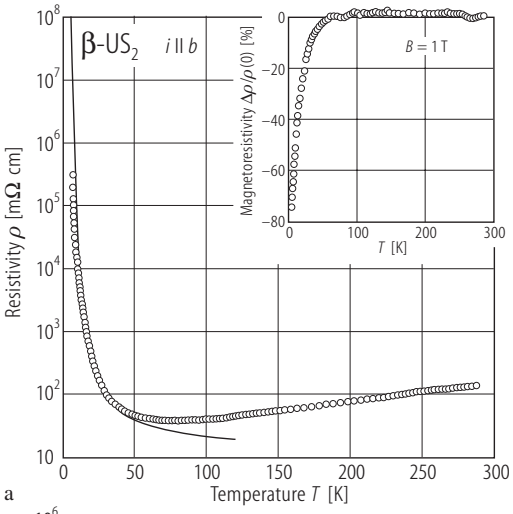

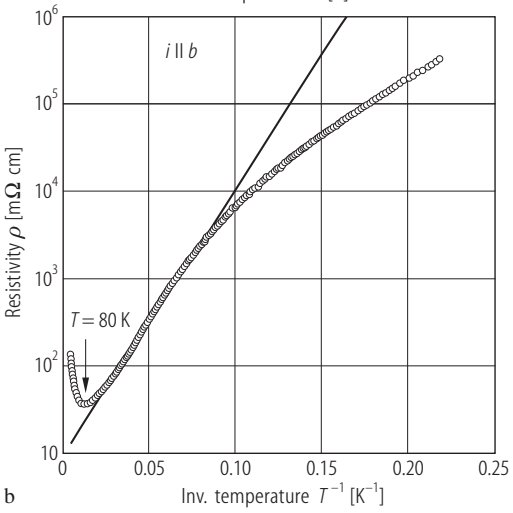

Fig. 389. β-US_2, sc. **(a)** Electrical resistivity, ρ, vs. temperature, T, measured with the current flowing along the b-axis [95S, 99ST]. The solid line is a fit of the experimental data in the range 12…50 K to the equation: $\rho(T)[\text{m}\Omega\text{cm}] = 10\exp(12.1\ \text{meV}/2k_B T)$. Inset: transverse magnetoresistivity, $\Delta\rho/\rho(0)$, vs. T, measured in a field of 1 T. Note a huge value of –76% at 4.2 K. **(b)** Resistivity, log ρ, vs. inverse temperature, T, measured as in panel **(a)** [99ST]. The solid line is a fit from panel **(a)**. Note that the energy gap ΔE_g = 12.1 meV is comparable to that reported in [72SGWC] for similar range of temperatures (see Fig. 388).

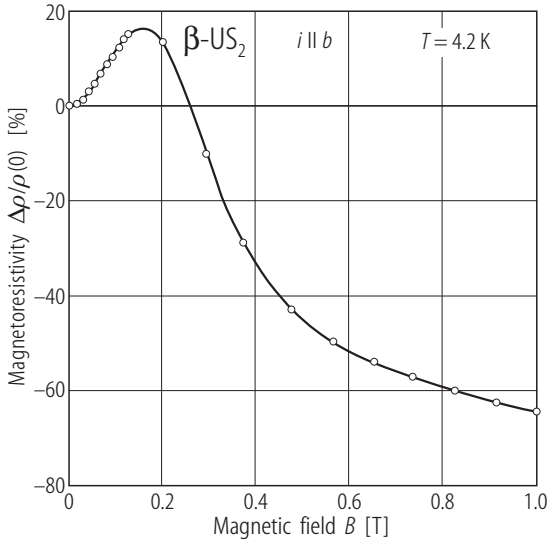

Fig. 390. β-US_2, sc. Transverse magnetoresistivity, $\Delta\rho/\rho(0)$, vs. magnetic field, B, measured at $T = 4.2$ K with the current flowing along the b-axis [99ST]. The maximum occurring near 0.2 T is reminiscent to the behaviour of metamagnets. However, in the magnetic studies β-US_2 was characterized as a paramagnet with a singlet ground state (see Figs. 386 and 387). Note a huge value of $\Delta\rho/\rho(0)$ at 1 T.

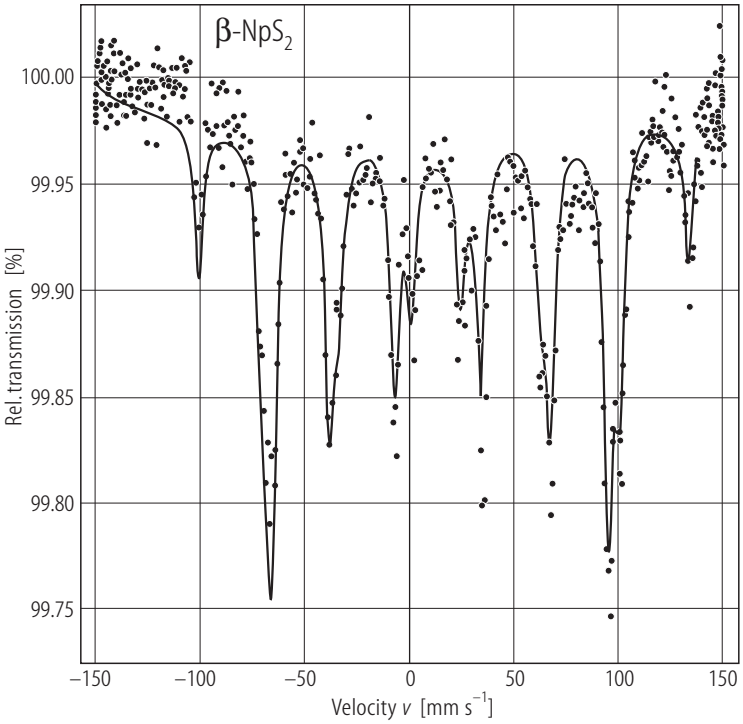

Fig. 391. β-NpS_2. ^{237}Np Mössbauer absorption spectrum taken at $T = 4.2$ K [84TJP]. The hyperfine parameters are presented in Table J. The isomer shift value evidences the tetravalent state of Np ions.

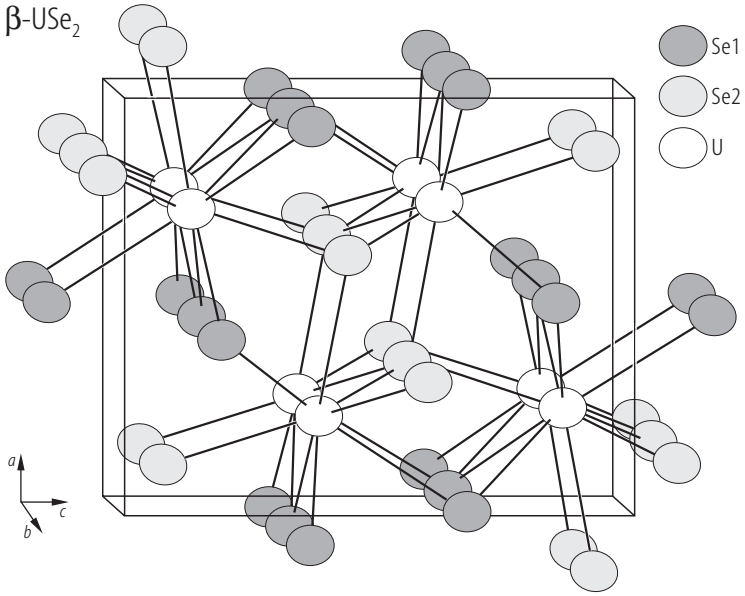

Fig. 392. β-USe_2. Orthorhombic crystal structure of the $PbCl_2$ type (space group Pnma) [96NPTS]. The uranium atoms are bonded to nine Se atoms, forming a tricapped trigonal prism. This structure was first described by [72SGWC] in space group Pnam.

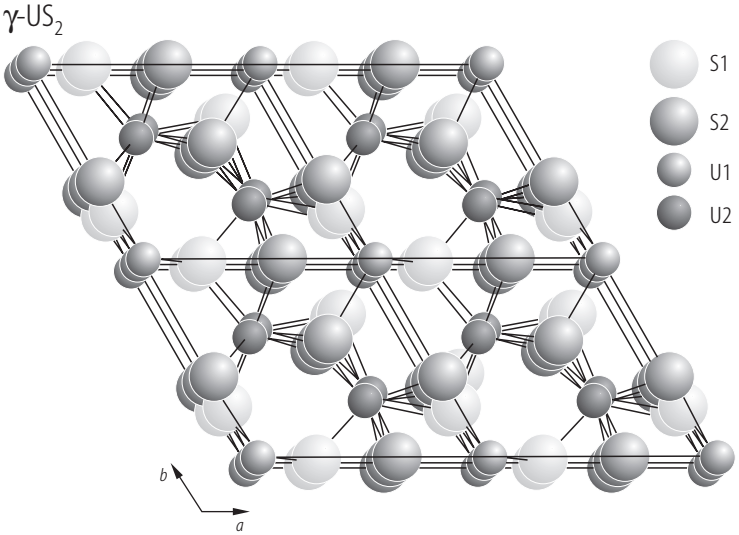

Fig. 393. γ-US_2. Hexagonal crystal structure of anti Fe_2P-type (space group $P\bar{6}2m$) projectedon the (*ab*)-plane [96DLPN]. Small circles: U1 atoms at the 1(a) sites and U2 atoms at the 2(d) sites; large circles: S. Light and dark shaded symbols denote the atoms with the positional parameter $z = 0$ and $z = 0.5$, respectively. Also γ-USe_2 was found to crystallize with this structure. For structural relationships see also [97KB].

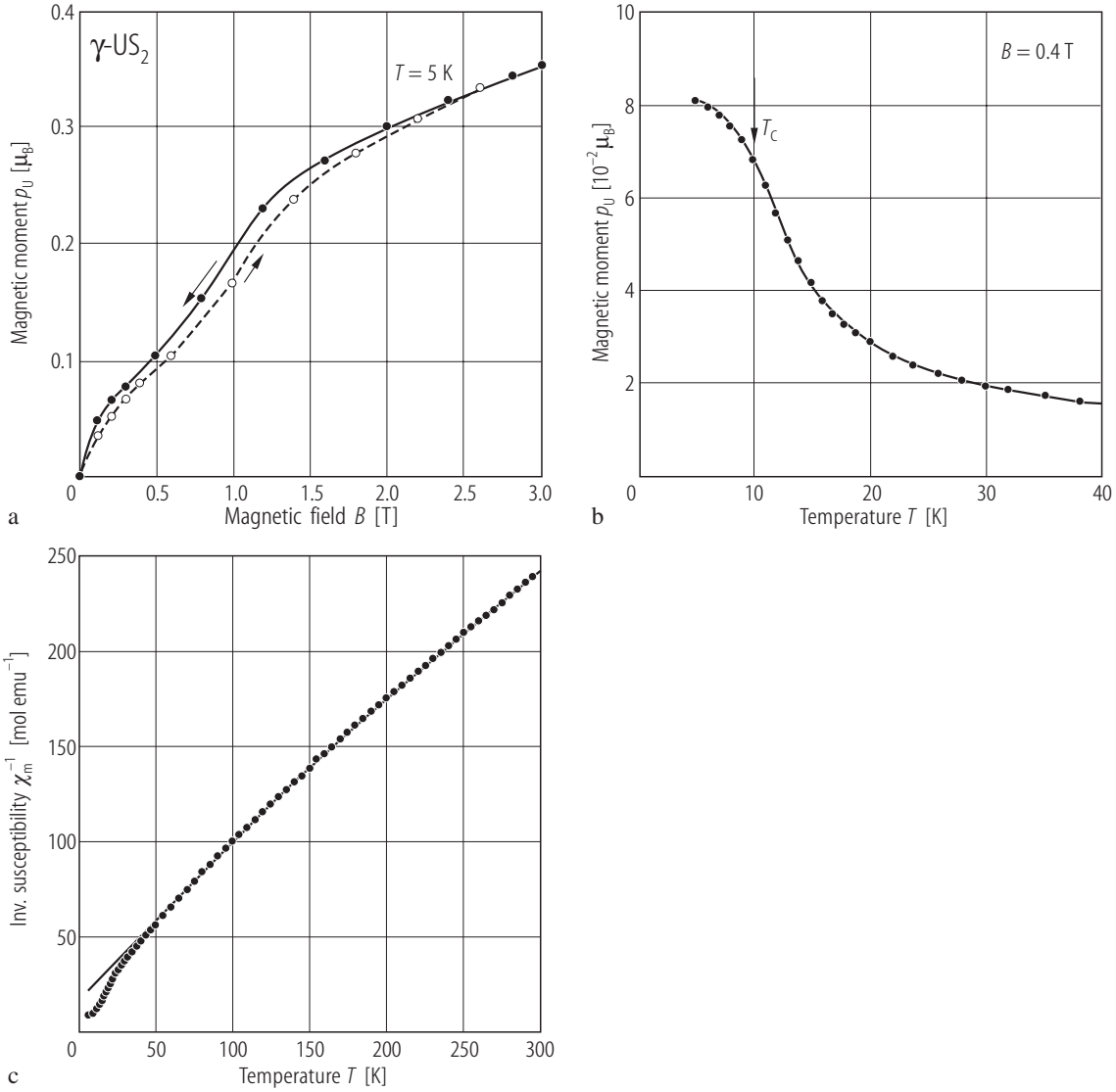

Fig. 394. γ-US_2. **(a)** Magnetic moment, p_U, vs. magnetic field, B, taken at T = 5 K with increasing (open circles) and decreasing (full circles) magnetic field [96DLPN]. **(b)** Magnetic moment, p_U, vs. temperature, T, below 40 K [96DLPN]. The compound exhibits weak ferromagnetism below T_C = 10 K, which probably originates from a noncollinear antiferromagnetic ordering. **(c)** Inverse molar magnetic susceptibility, χ_m^{-1}, vs. temperature, T, measured in a field of 0.4 T [96DLPN]. The solid line is a modified Curie-Weiss fit with the parameters given in Table F.

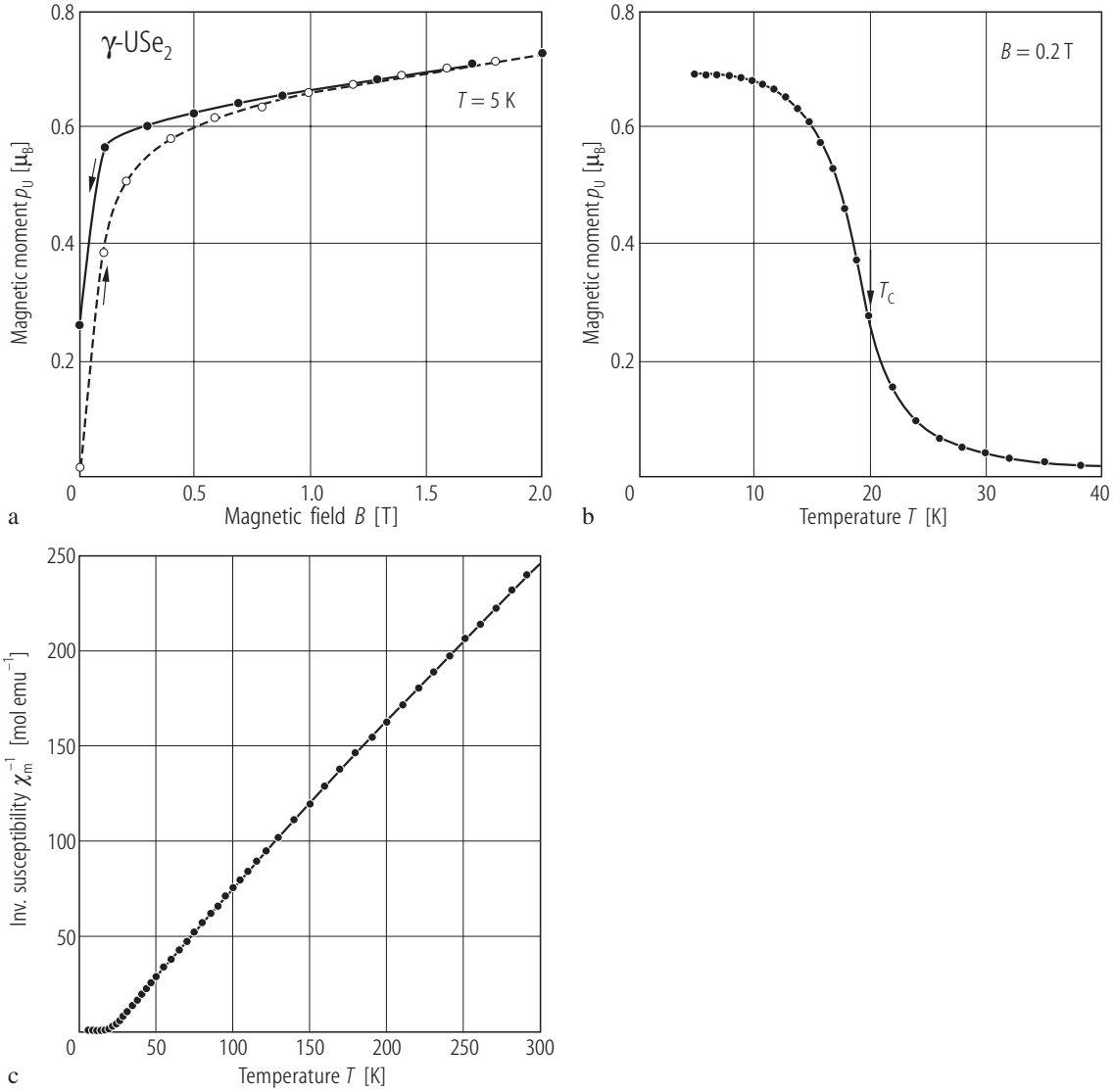

Fig. 395. γ-USe_2. **(a)** Magnetic moment, p_U, vs. magnetic field, B, taken at T = 5 K with increasing (open circles) and decreasing (full circles) magnetic field [96DLPN]. **(b)** Magnetic moment, p_U, vs. temperature, T below 40 K [96DLPN]. T_C = 20 K; p_s = 0.72 μ_B/U atom. **(c)** Inverse molar magnetic susceptibility, χ_m^{-1}, vs. temperature, T, measured in a field of 0.4 T [96DLPN]. The solid line is a modified Curie-Weiss fit with the parameters given in Table F.

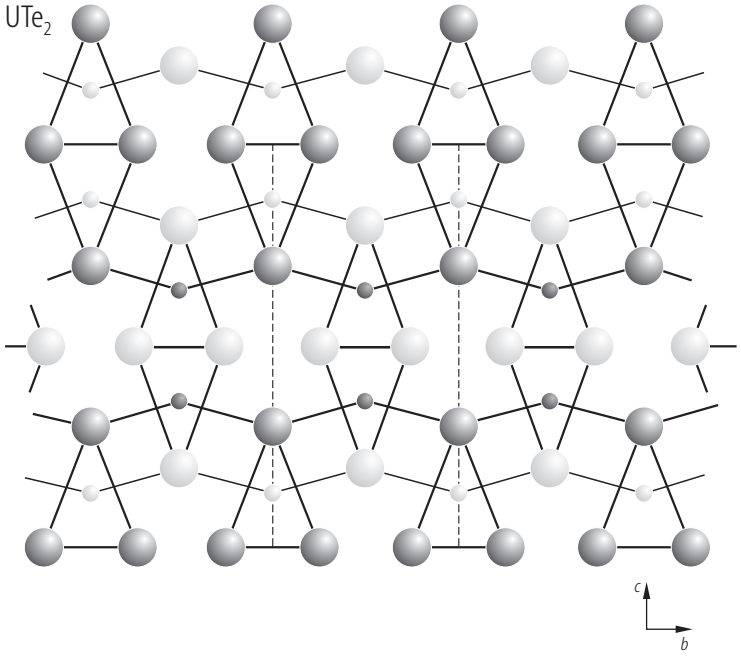

Fig. 396. UTe_2. Orthorhombic crystal structure (space group Immm) projected on the (*bc*)-plane [88BD]. Small circles: U; large circles: Te. Light and dark shaded symbols denote the atoms with the positional parameter $x = 0$ and $x = 0.5$, respectively. The structure is built up by bicapped trigonal prisms of Te atoms, connected by faces to fourfold capped biprisms.

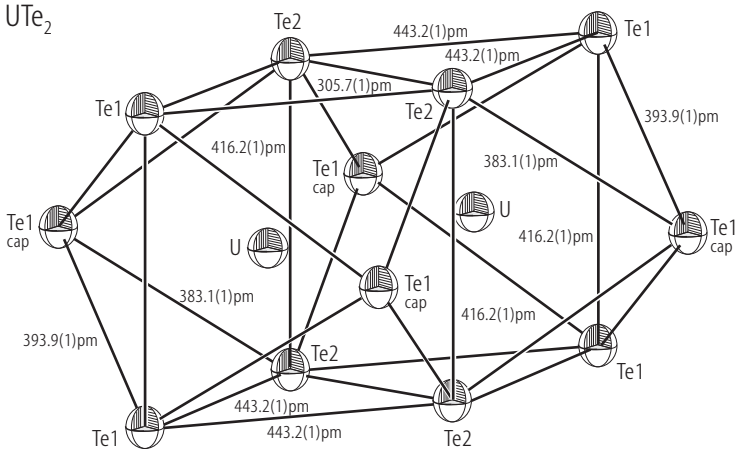

Fig. 397. UTe_2. Coordination polyhedra around the U atoms placed in the fourfold-capped biprisms [96S3]. The numbers are the interatomic distances at room temperature.

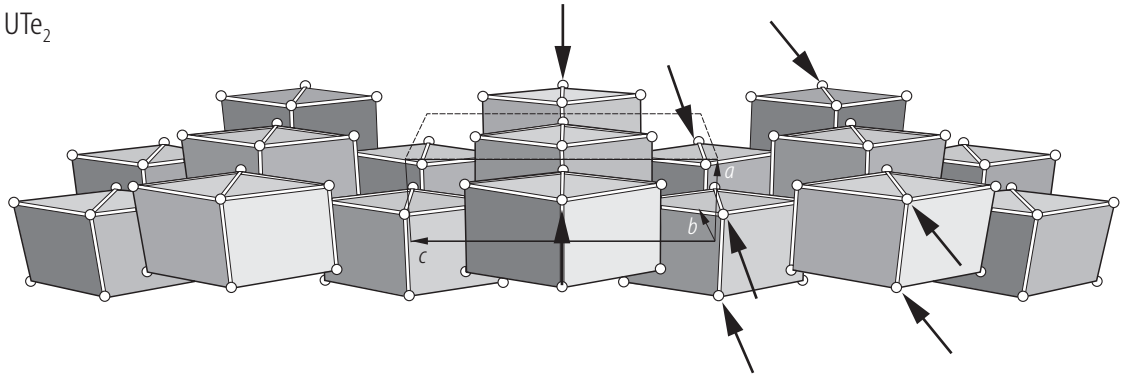

Fig. 398. UTe_2. Crystal structure in a [010] projection (tilted by ca. 30º) [97S2]. For a sake of clarity the prism caps (see Fig. 396) were omitted. The arrows mark linear tellurium atom chains.

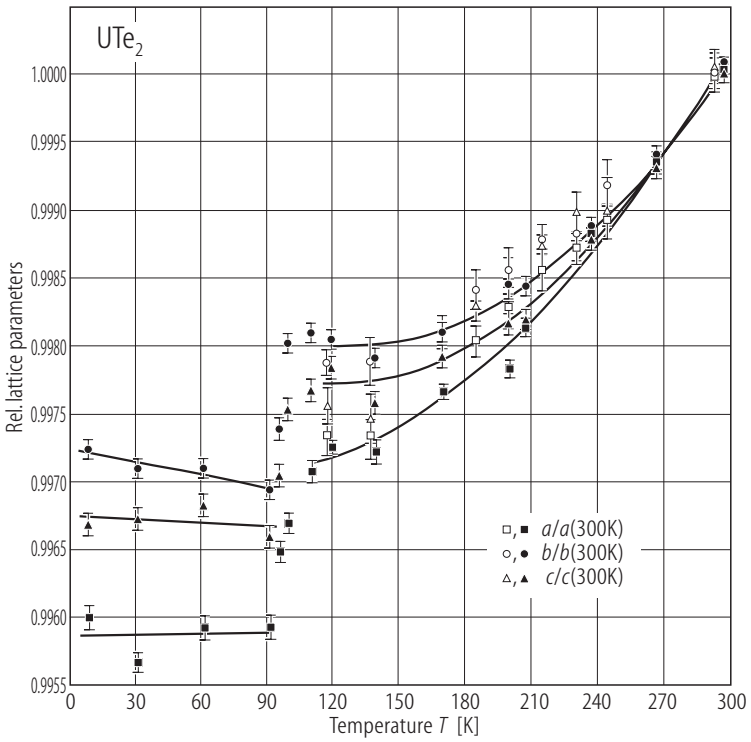

Fig. 399. UTe_2. Relative lattice parameters, a/a(300K), b/b(300K), c/c(300K), vs. temperature, T, in the range 10…293 K [97S2]. Open symbols: single crystal data; full symbols: powder data. A sudden change in the lattice parameters between 92 and 110 K is not accompanied by a symmetry change and is uniform in the three directions. A nature of this transformation is unclear as yet.

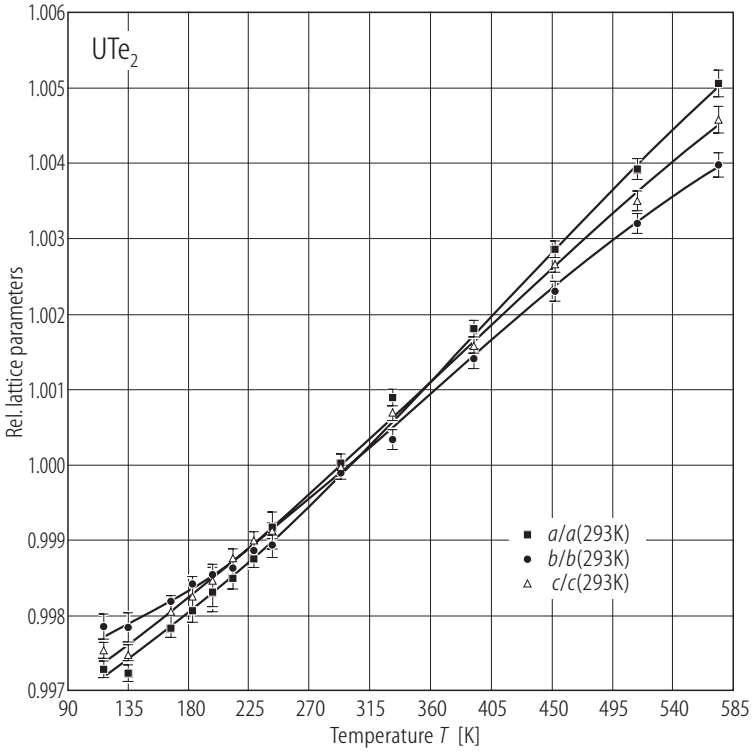

Fig. 400. UTe_2, sc. Relative lattice parameters, a/a(293K), b/b(293K), c/c(293K), vs. temperature, T, in the range 118…573 K [96S3]. There are no anomalies, which would indicate a change in the orthorhombic structure. The thermal contraction is very similar in all three directions.

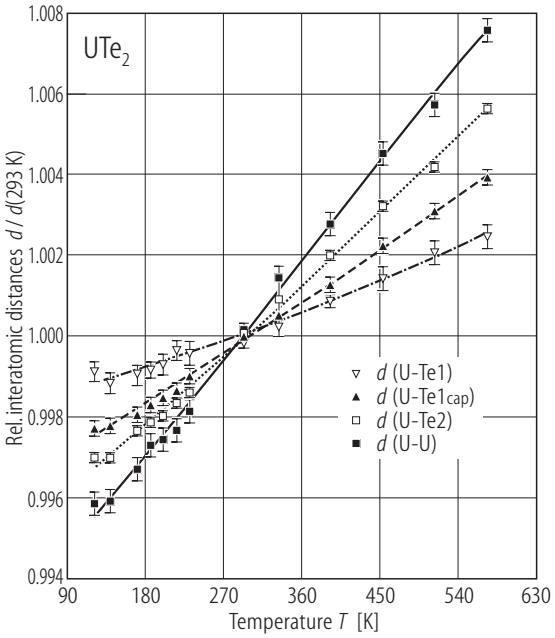

Fig. 401. UTe_2, sc. Relative interatomic distances, $d/d(293K)$, vs. temperature, T, in the range 118…573 K [96S3]. The U-Te1 distance is only slightly temperature dependent, whereas the U-U distance considerably decreases with lowering temperature.

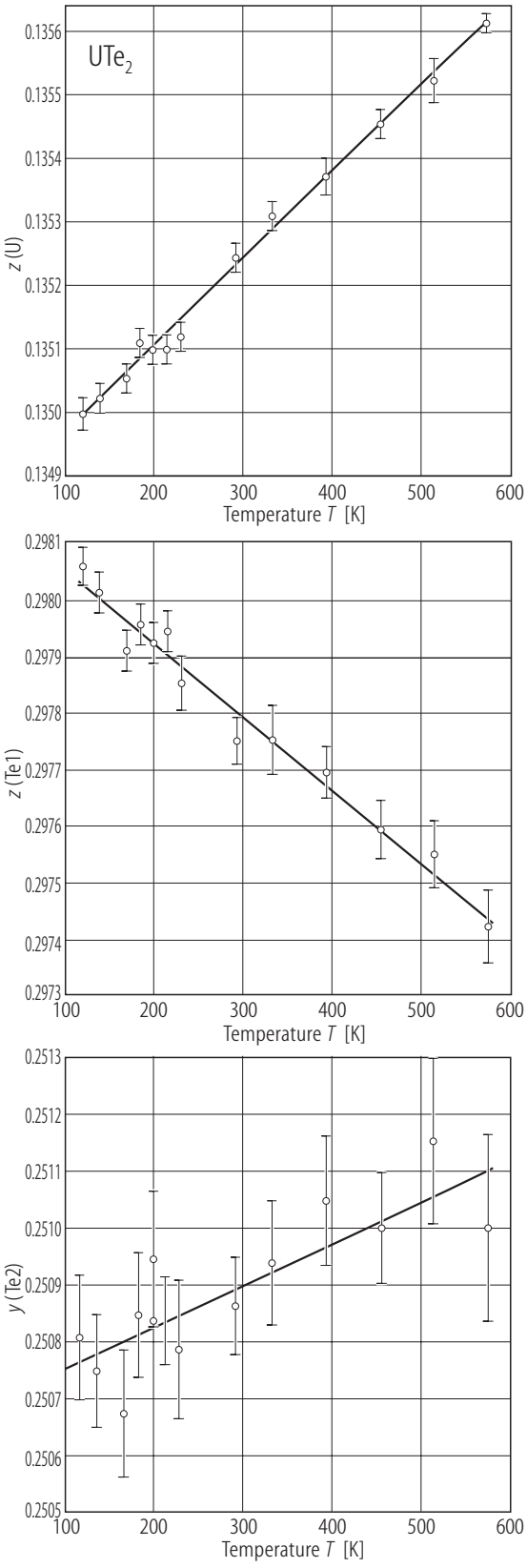

Fig. 402. UTe_2, sc. Positional parameters, z(U), z(Te1), y(Te2), vs. temperature, T, in the range 118…573 K [96S3]. The increase in z(Te1) with decreasing temperature compensates the thermal contraction of the lattice parameters (see Fig. 400) and as a result the U-Te1 distance is almost independent of temperature (see Fig. 401).

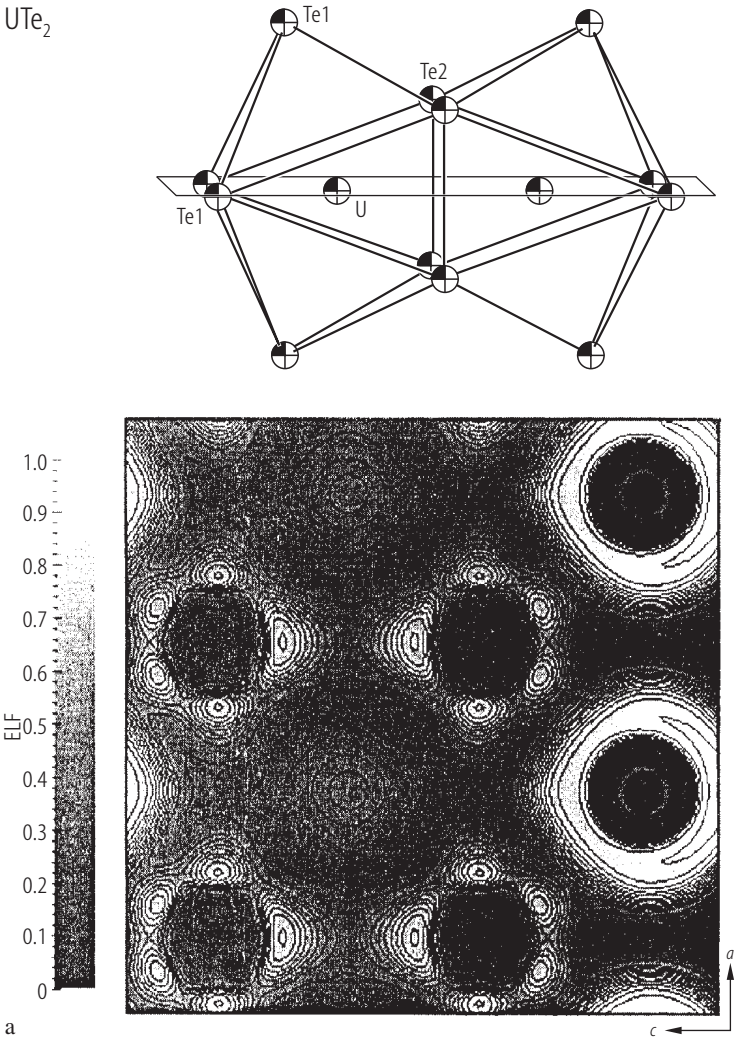

Fig. 403a. For caption see next page

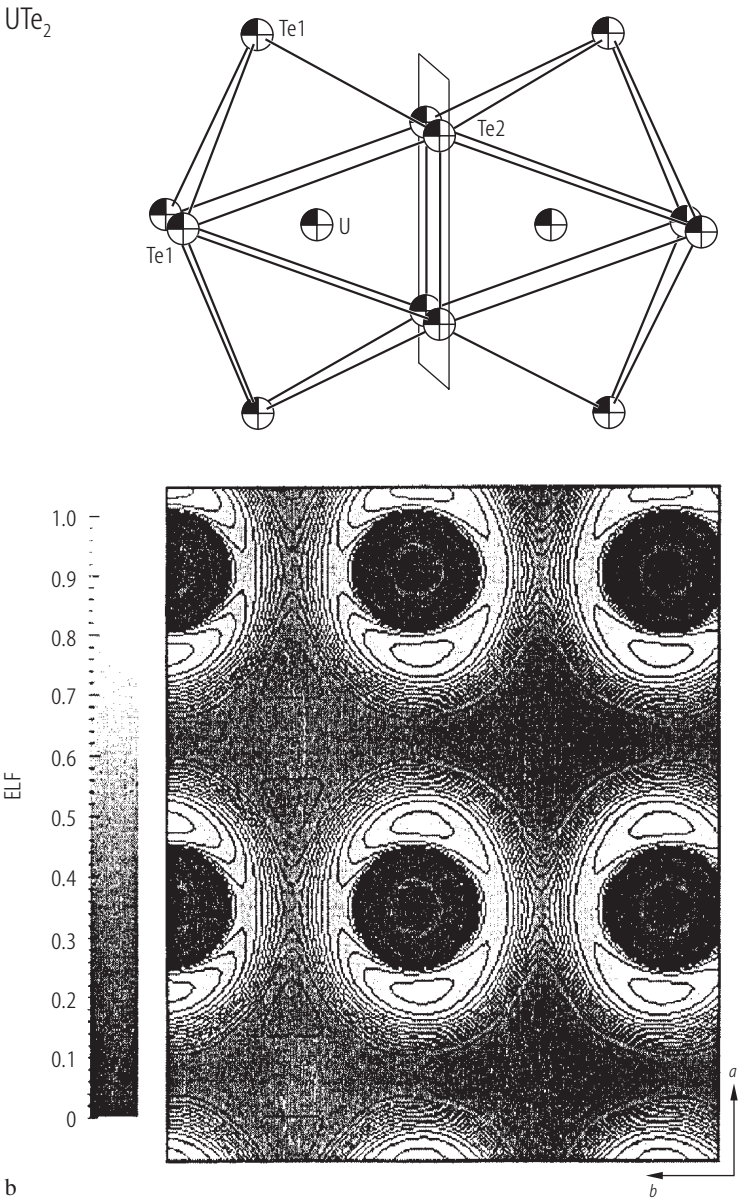

Fig. 403. UTe_2. Electron localization function maps in the sections through the characteristic planes: **(a)** ($x0z$); **(b)** ($xy0$) [97S2]. The sections are schematically shown above the maps. For description of the topological procedure see the original paper. From the analysis of the local ELF maxima and their basins it is deduced the presence of two different Te atoms and proposed the valence electron distribution according to the formula $U^{1.9+}Te^{1.2-}Te^{0.7-}$.

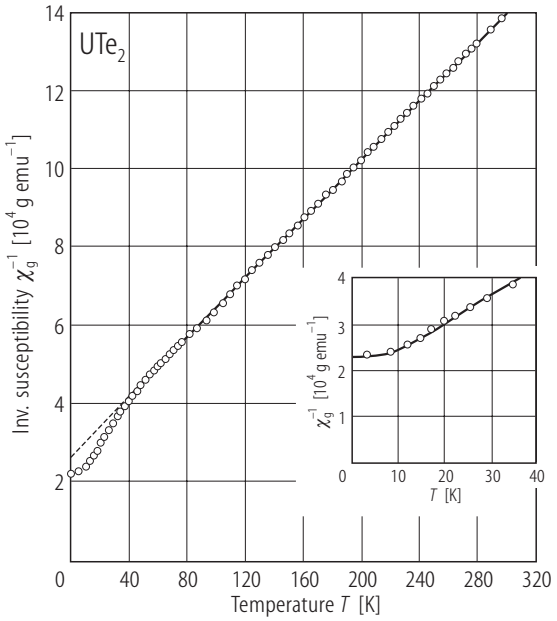

Fig. 404. UTe_2. Inverse mass magnetic susceptibility, χ_g^{-1}, vs. temperature, T [79NT]. The compound remains paramagnetic down to 4.2 K. The dashed line is a Curie-Weiss fit with the parameters given in Table F. Inset: low temperature $\chi_g^{-1}(T)$ [79NT]. A leveling-off observed below 10 K is characteristic of nonmagnetic ground state (singlet).

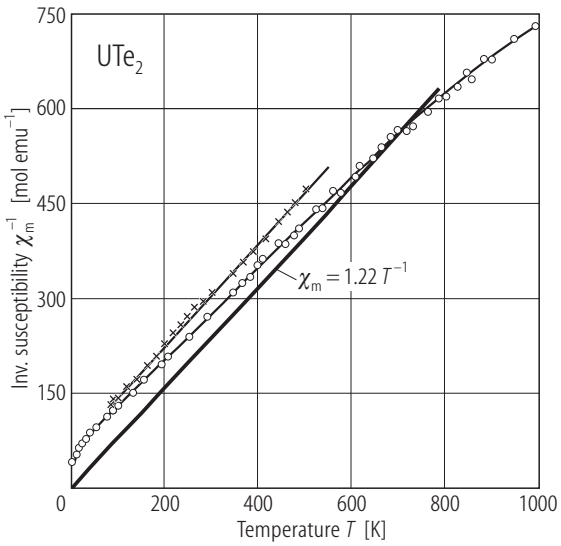

Fig. 405. UTe_2. Inverse molar magnetic susceptibility, χ_m^{-1}, vs. temperature, T, in the range 4.2…1000 K [72S, 73S]. For comparison the results taken from [67CPYM] are shown by crosses. The bold straight line is a Curie law with p_{eff} = 3.1 μ_B. Note a lack of saturation in $\chi_m^{-1}(T)$ at low temperatures, inconsistent with the more recent finding by [79NT] (compare Fig. 404).

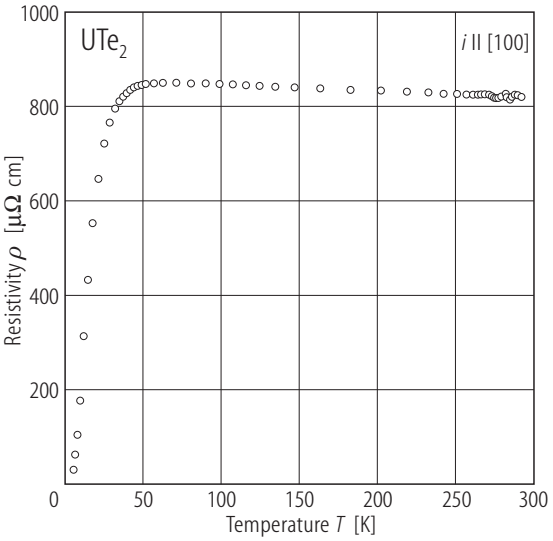

Fig. 406. UTe_2, sc. Electrical resistivity, ρ, vs. temperature, T, measured with the current flowing along the a-axis [95S, 99ST]. Note that in contrast to other uranium dichalcogenides UTe_2 exhibits semimetallic properties. Above 50 K the resistivity is Kondo like. At lower temperatures the resistivity rapidly decreases due to setting in a coherent state (the compound is nonmagnetic).

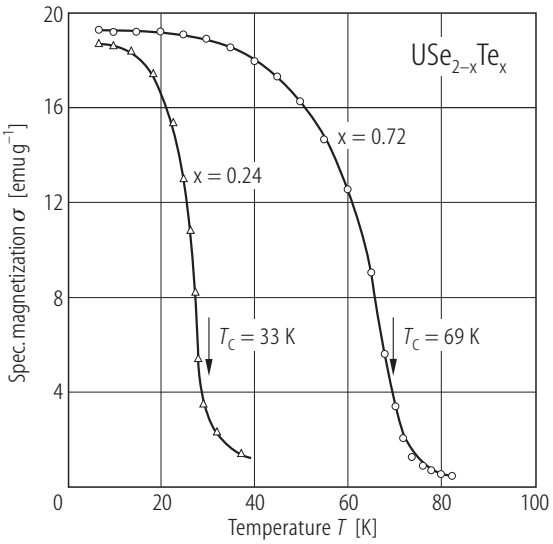

Fig. 407. $USe_{2-x}Te_x$. Thermomagnetic curves taken at B = 0.2 T for x = 0.24 and 0.72 [96NPTS]. T_C = 33 and 69 K, respectively. The ferromagnetic properties of these mixed uranium dichalcogenides contrast with a nonmagnetic behaviour of pure UTe_2 (compare Fig. 404).

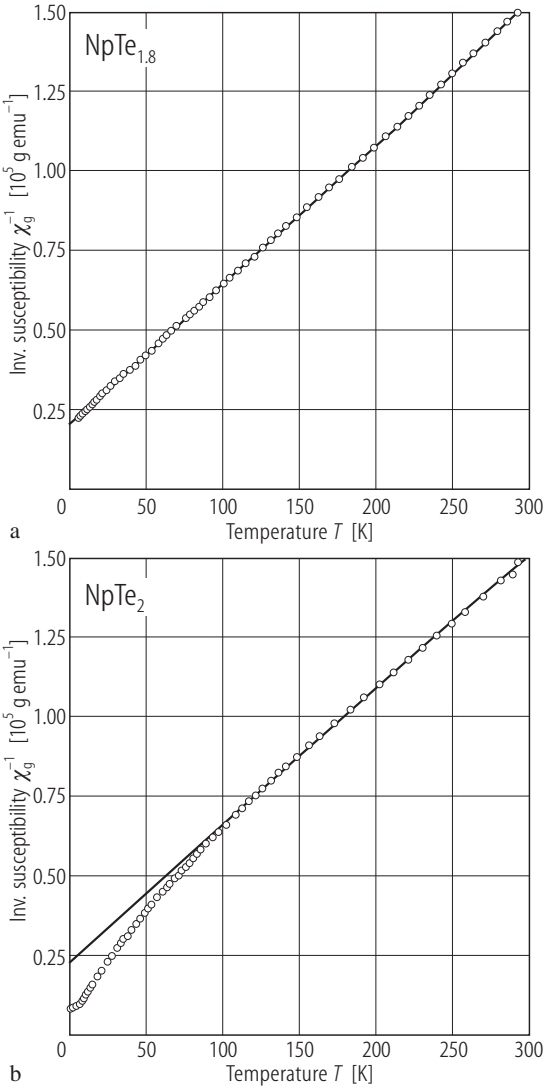

Fig. 408. $NpTe_{2-x}$. Inverse mass magnetic susceptibility, χ_g^{-1}, vs. temperature, T, for **(a)** $NpTe_{1.8}$ and **(b)** $NpTe_2$ [82BFDC]. Both compounds remain paramagnetic down to 2 K. The solid lines are Curie-Weiss fits with the parameters given in Table F. In the case of $NpTe_2$ $\chi_g^{-1}(T)$ shows a strong curvature below 140 K, which evidences crystal field interactions being weaker than in $NpTe_{1.8}$. A tendency towards saturation below 6 K is attributed to the presence of a singlet ground state.

For Fig. 410 see next page

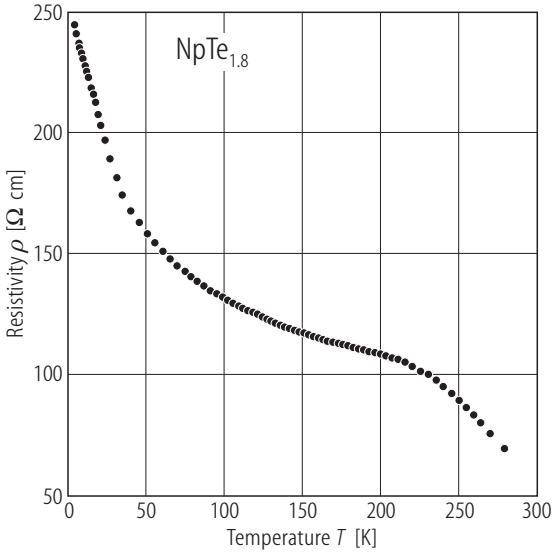

Fig. 409. $NpTe_{1.8}$. Electrical resistivity, ρ, vs. temperature, T [82BFDC]. Large values of the resistivity and its increase with decreasing temperature suggest semiconducting properties.

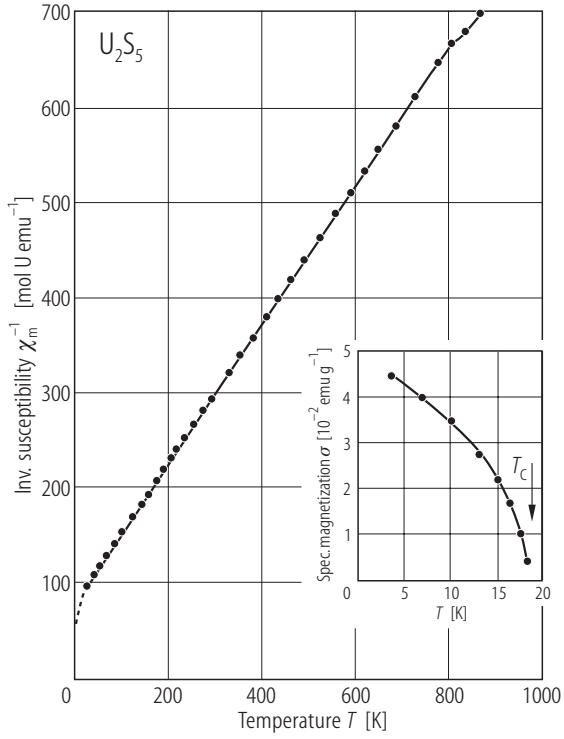

Fig. 411. U_2S_5. Inverse molar magnetic susceptibility, χ_m^{-1}, vs. temperature, T, in the range 4.2…900 K [80N]. Above 30 K the Curie-Weiss law is followed with the parameters given in Table F. Inset: Specific magnetization, σ, vs. T below 19 K. The compound shows a weak ferromagnetism below T_C = 18 K.

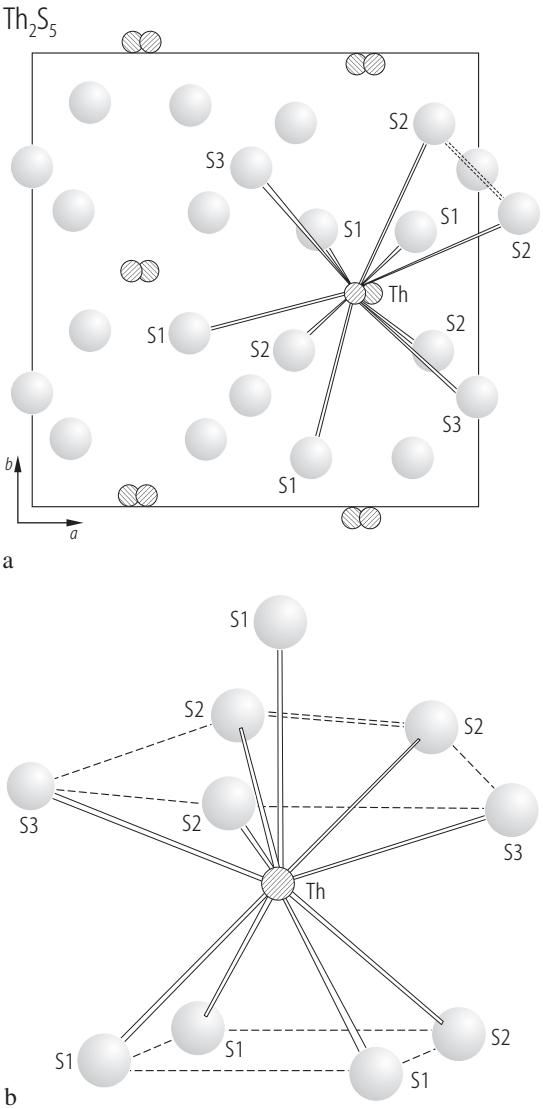

←

Fig. 410. Th_2S_5. **(a)** Orthorhombic crystal structure (space group Pcnb) projected on the (*ab*)-plane [82NP]. Dashed circles: Th; large circles: S. Emphasized is the coordination of Th atom by ten sulphur atoms. See [99KB] for the detailed description of this type of structure for the case of Th_2Se_5. **(b)** Th atom coordination polyhedron [82NP]. A very short S2-S2 distance of 211.7(7) pm indicates that the compound is a polysulphide having $(S{=}S)^{2-}$ ions.

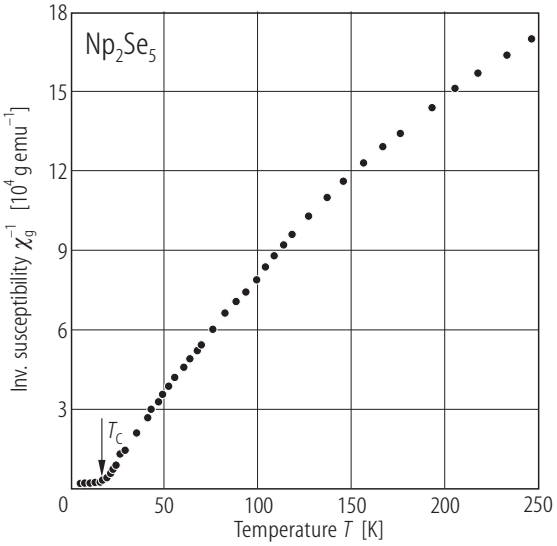

Fig. 412. Np_2Se_5. Inverse mass magnetic susceptibility, χ_g^{-1}, vs. temperature, T [82TPW]. The compound orders ferromagnetically at T_C = 15 K.

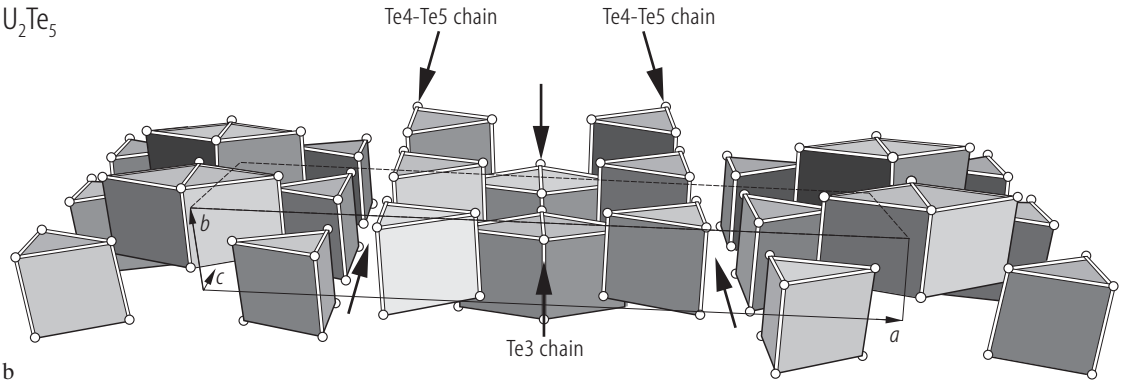

Fig. 413b. For caption see next page

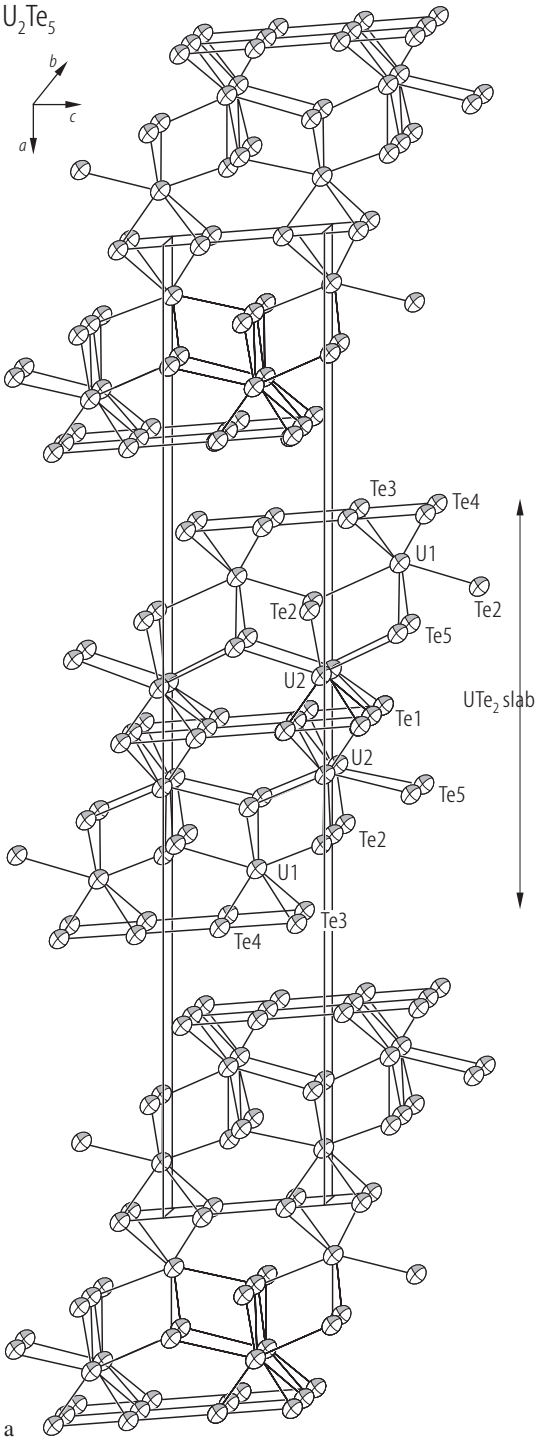

Fig. 413. U_2Te_5. **(a)** Monoclinic crystal structure (space group C2/m) [96S2, 97TPPN]. There are in the unit cell the UTe_2 slabs built up along the *a*-axis separated by van der Waals gaps and forming a layered type structure. **(b)** Crystal structure projected along the [010] axis and tilted by an angle of 30° [96S2]. For simplification the prism caps were omitted. Examples of linear Te chains are marked by arrows. In total there are as many Te4-Te5 chains as Te3 chains. Two nonequivalent U atoms are coordinated to eight Te atoms in a bicapped trigonal prismatic polyhedra.

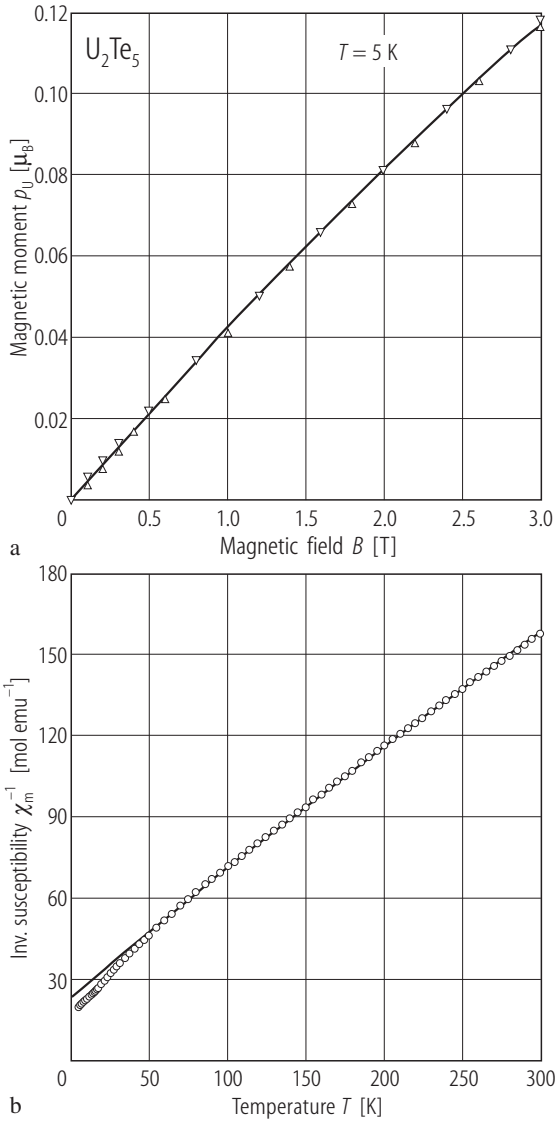

Fig. 414. U_2Te_5. **(a)** Magnetic moment, p_U, vs. magnetic field, *B*, taken at *T* = 5 K [97TPPN]. **(b)** Inverse molar magnetic susceptibility, χ_m^{-1}, vs. temperature, *T*, measured in a field of 0.4 T [97TPPN]. The solid line is a modified Curie-Weiss fit with the parameters given in Table F. The deviation of $\chi_m^{-1}(T)$ from the MCW behaviour below 60 K probably results from crystal field interactions. The compound is paramagnetic down to 2 K.

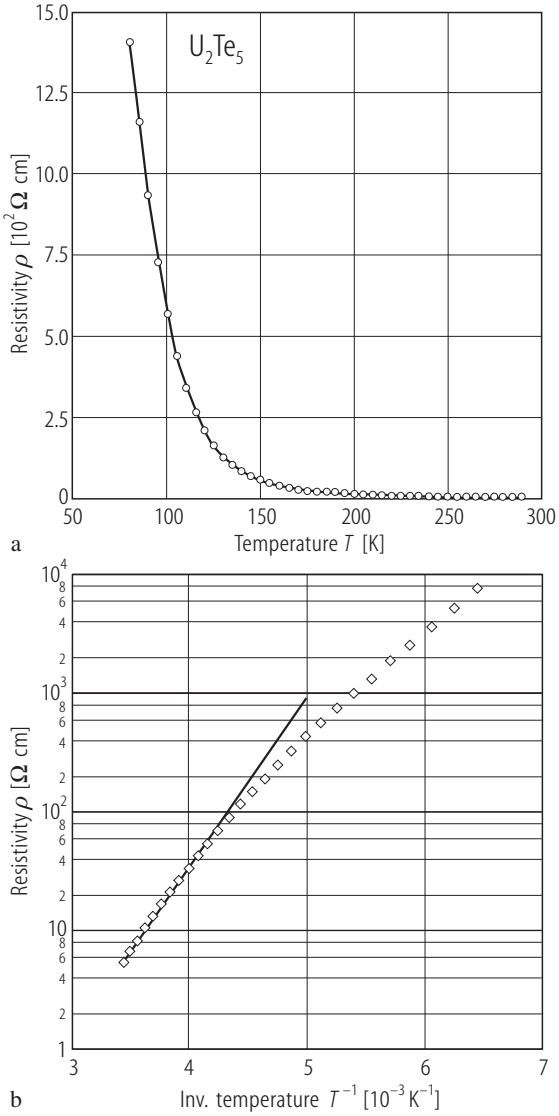

Fig. 415. U_2Te_5, sc. **(a)** Electrical resistivity, ρ, vs. temperature, T, measured in an undefined direction [97TPPN]. ρ(300K) = 2.05 Ωcm. Note a semiconducting behaviour. **(b)** Resistivity plotted as log ρ vs. 1000/T [97TPPN]. The solid line is a fit of the experimental data in the temperature range 230…300 K to the activation law with E_g = 30(10) meV.

For Fig. 416 see next page

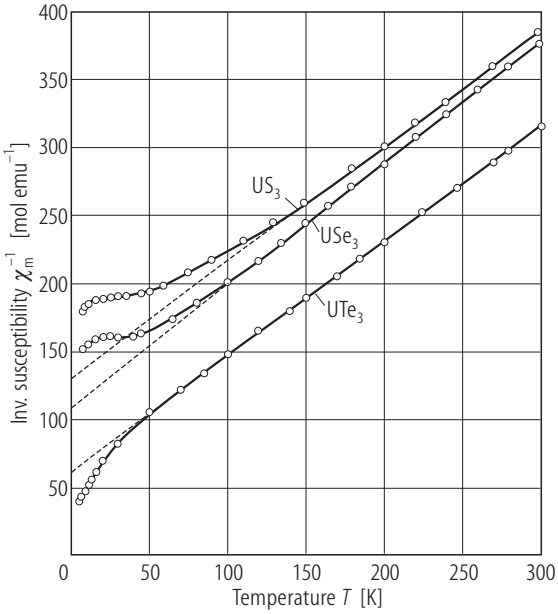

Fig. 417. UY_3, Y = S, Se, Te. Inverse molar magnetic susceptibility, χ_m^{-1}, vs. temperature, T, measured on powdered single crystals [86N]. The dashed lines denote Curie-Weiss fits with the parameters given in Table F.

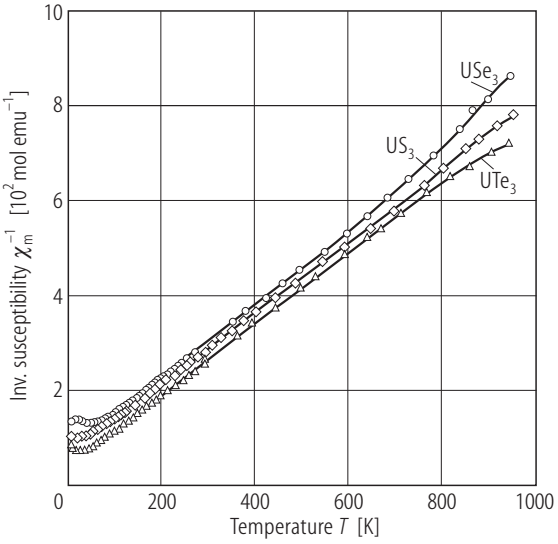

Fig. 418. UY_3, Y = S, Se, Te. Inverse molar magnetic susceptibility, χ_m^{-1}, vs. temperature, T, in the range 4.2…950 K [76S]. Compare these dependencies with those shown in Fig. 417.

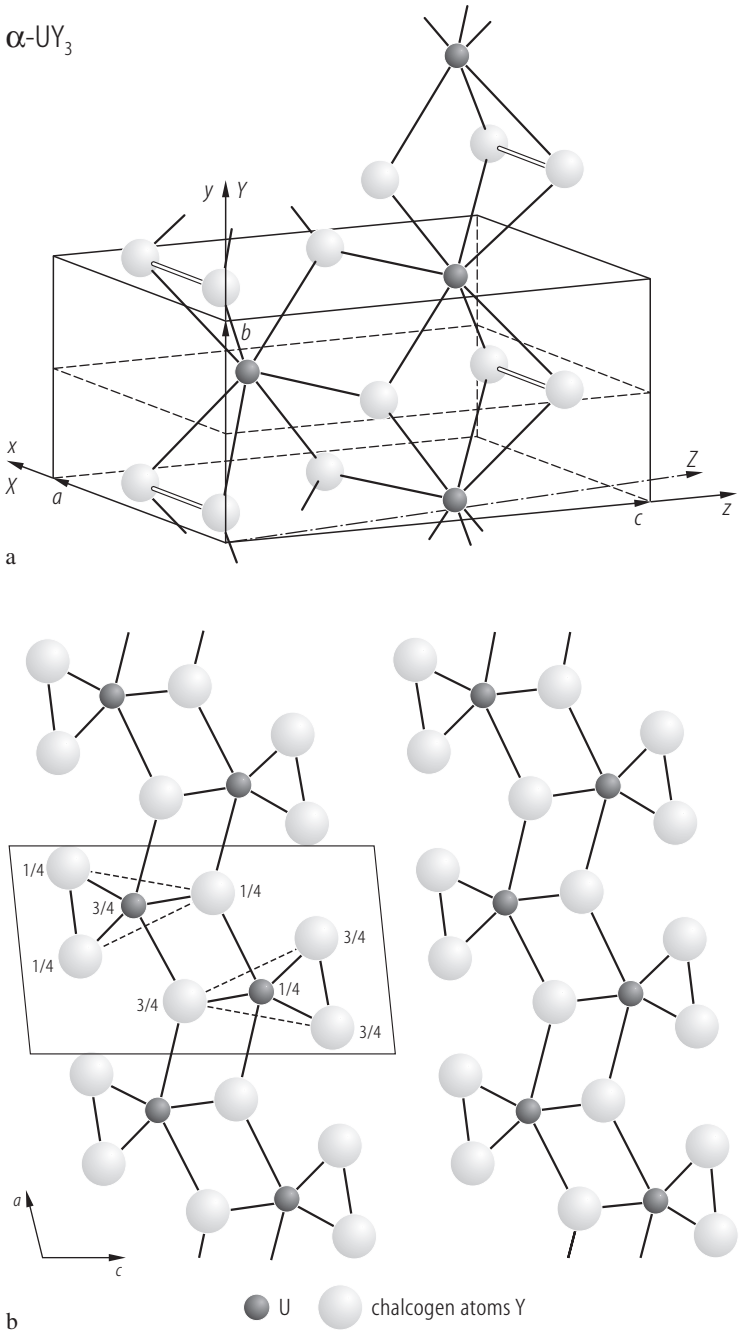

Fig. 416. UY_3, Y = S, Se, Te. **(a)** Spatial view of the monoclinic crystal structure of ZrS_3-type (space group $P2_1/m$) and bonding scheme [75FBK, 87NZRL]. The unit cell contains two molecular units. A chain characteristic of the structure running along the *b*-axis is also shown. **(b)** Projection of the structure along the *b*-axis [86N]. Uranium atom is at the centre of trigonal prism of chalcogen atoms, which form linear chains parallel to the *b*-axis. The chains are interconnected by U-Y bonds forming the (001) layers. These layers are stacked along the *c*-axis by van der Waals bonds between the Y atoms.

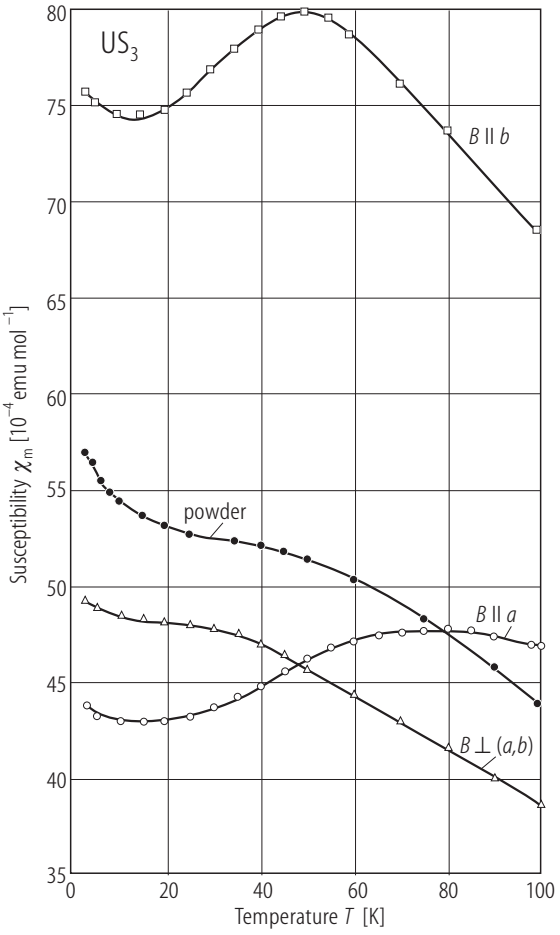

Fig. 419. US_3, sc. Molar magnetic susceptibility, χ_m, vs. temperature, T, in the range 2…100 K, measured with magnetic field applied along the a-axis (open circles), along the b-axis (open squares) and perpendicular to the (ab)-plane (open triangles), as well as on a powder sample (full circles) [86N]. Note a large anisotropy related to the anisotropy of the monoclinic crystal structure. Broad maxima in $\chi_m(T)$, centered for $B \parallel a$ at 80 K and for $B \parallel b$ at 50 K, indicate a two-dimensional character of short range magnetic interactions with the magnetic moments probably aligned parallel to the chain axis b (see Fig. 416).

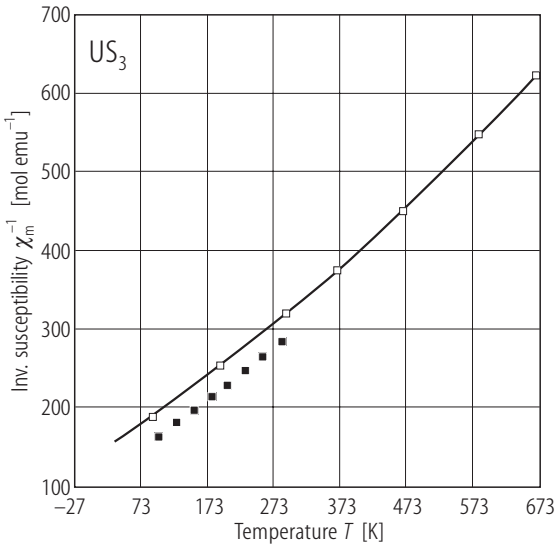

Fig. 420. US_3. Inverse molar magnetic susceptibility, χ_m^{-1}, vs. temperature, T, in the range 80…750 K (open squares) [68GHTT]. For comparison the data obtained by [61TS] and [64ST] between 80 and 300 K are shown by full squares. The effective magnetic moment p_{eff} is 3.14 and 3.43 μ_B for these two studies, respectively.

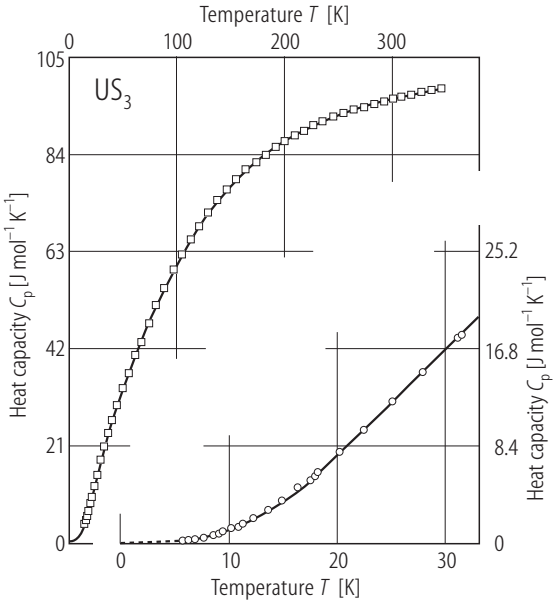

Fig. 421. US_3. Heat capacity, C_p, vs. temperature, T, in the range 5…350 K (upper and left-hand side scales) and 5…30 K (bottom and right-hand side scales) [68GW]. Note the absence of cooperative phenomena down to 5 K.

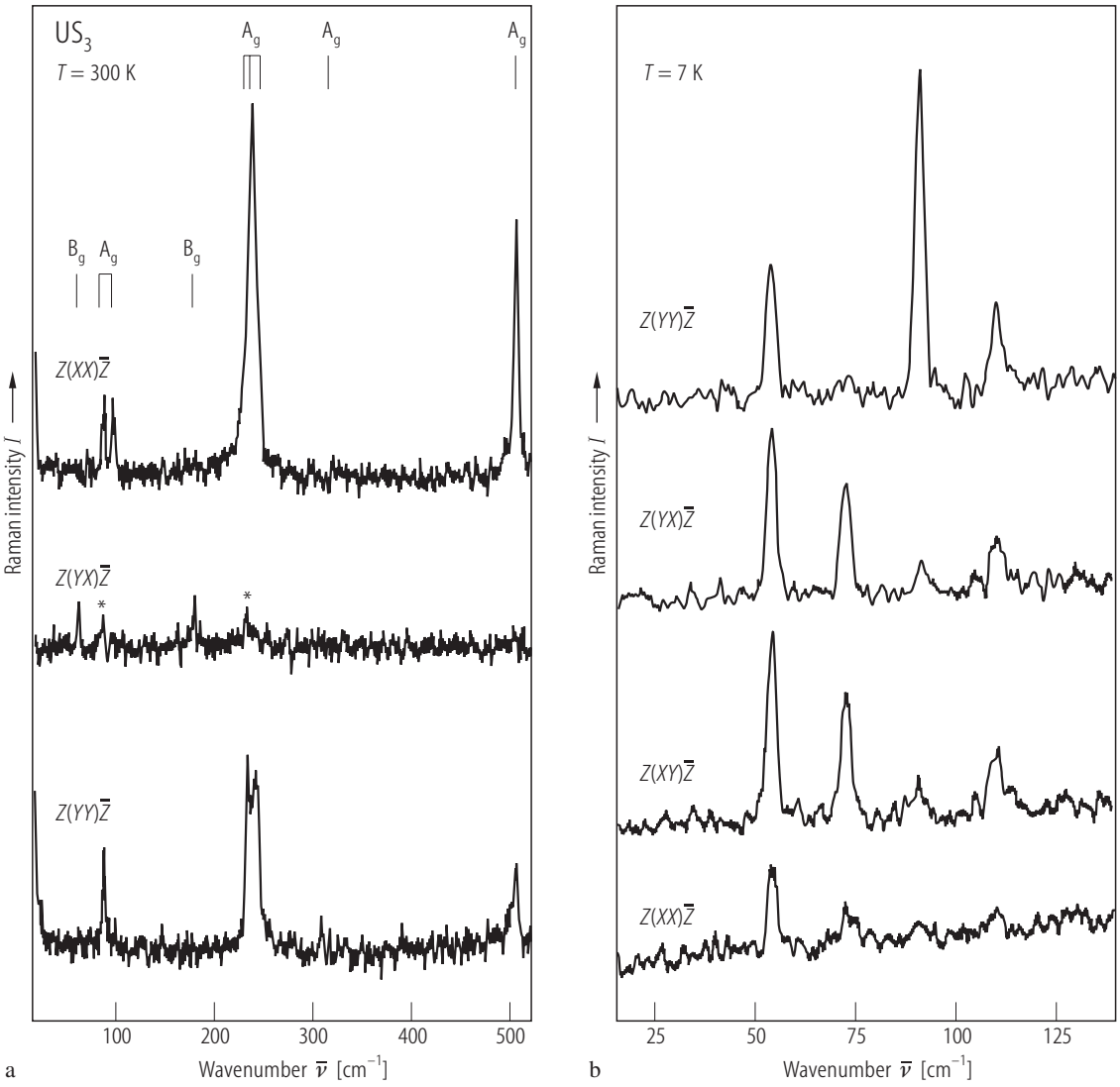

Fig. 422. US_3, sc. Raman spectra taken at **(a)** $T = 300$ K and **(b)** $T = 7$ K, excited with the $\lambda = 488.0$ pm laser line [86NZRN, 87NZRL]. The curves correspond to three different polarization configurations (two diagonal *XX*, *YY* and one off-diagonal *YX*) given by the labels $k_i(e_i e_s)k_s$, where *k* is the wave vector and *e* is the polarization of the light inside the crystal. The indices i and s refer to the incident and scattered light, respectively. The asterisks in panel **(a)** mark lines appearing in forbidden polarizations due to depolarization effects. The upper labels give the symmetry properties of the observed excitations. The A_g and B_g modes are classified according to displacements either in the mirror plane or out of it. There are 12 such modes, namely $\Gamma_R = 8A_g + 4B_g$. The A_g symmetry is assigned to phonons at 88, 98, 234, 239.5, 243, 297 and 506 cm^{-1}. The mode at 506 cm^{-1} is the stretching mode of S_2 diatomic "molecules". The low frequency A_g modes at 88 and 98 cm^{-1} involve translational and/or librational motions of adjacent chains one against the other. The A_g modes in the 234…297 cm^{-1} window correspond to an internal deformation of the chains. One of the two weak lines at 53 and 62 cm^{-1}, as well as the phonon responsible for the structure at 180 cm^{-1} are described as the B_g modes. In turn, the spectra taken at 7 K (panel **(b)**) display four sharp, equally spaced lines at 54, 72.5, 91 and 109.5 cm^{-1}, which are ascribed to electronic excitations within the $5f^2$ configuration of U^{4+} ion (see Fig. 423). See also Table W.

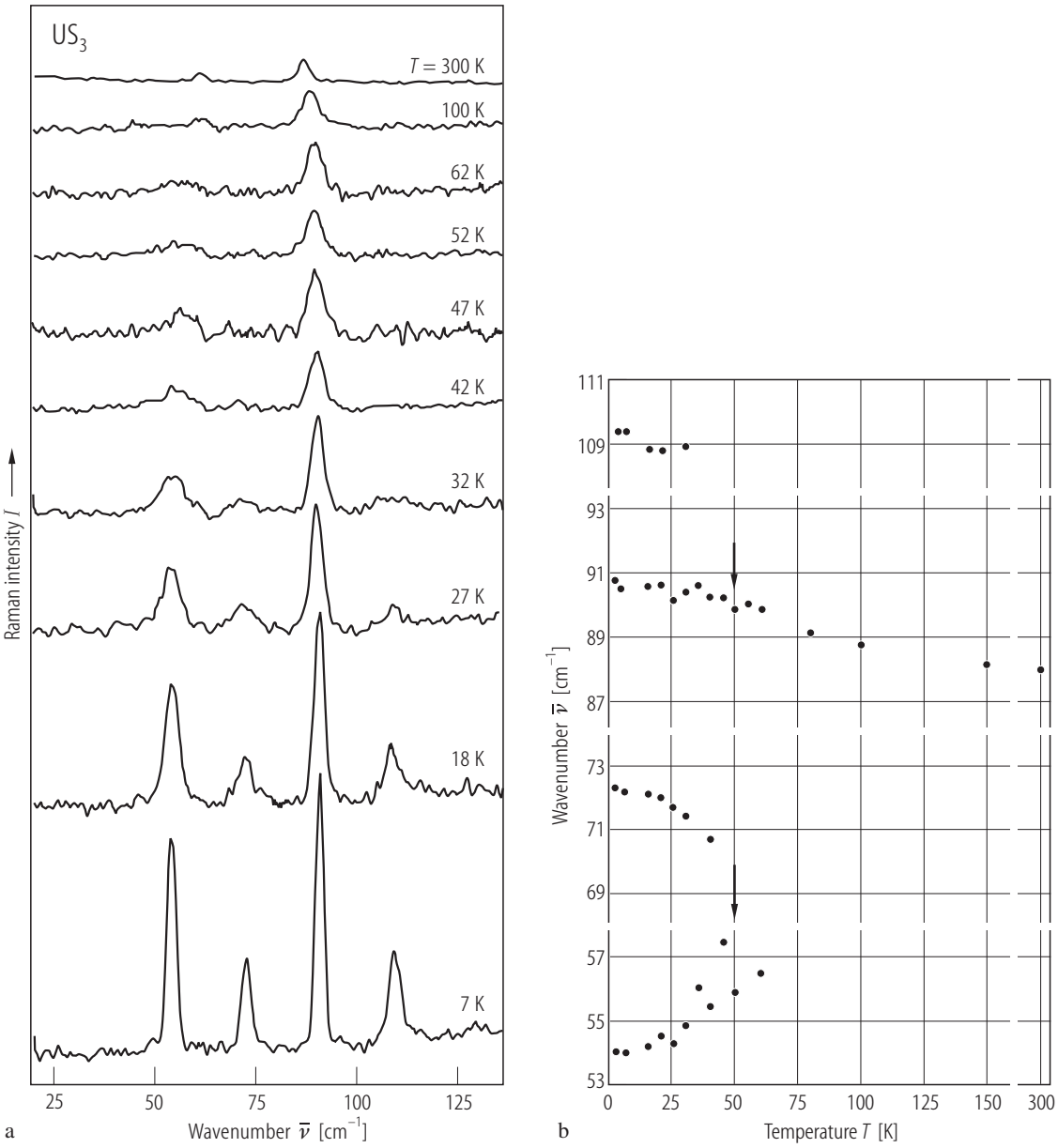

Fig. 423. US_3, sc. **(a)** Raman spectra taken at various temperatures in the range 7…300 K with $\lambda = 488.0$ pm light polarized parallel to the chains inside the crystal [86NZRN, 87NZRL]. Note a drastic change in the intensities upon decreasing temperature, which gives evidence for an antiferromagnetic order setting in below 50 K. The four equally spaced lines visible at low temperatures are attributed to electronic excitations within the $5f^2$ configuration of U^{4+} ion and have some magnetic contributions which are consistent with two-dimensional antiferromagnetic ordering (see Fig. 419). The stronger line at 91 cm^{-1} being still visible at 100 K merges into a phonon line at higher temperatures. On rising the temperature the bands broaden and their intensity decreases but without marked shift in the position. **(b)** Positions of the lines from panel **(a)** vs. temperature, T [86NZRN, 87NZRL]. The arrows mark the temperature T_{max} corresponding to the maximum in the magnetic susceptibility (see Fig. 419). Note that the line frequencies hardly shift over the temperature range studied, which precludes an assignment to magnon Raman scattering and suggests that the lines are electronic transitions within the $^3H_4$ ground multiplet.

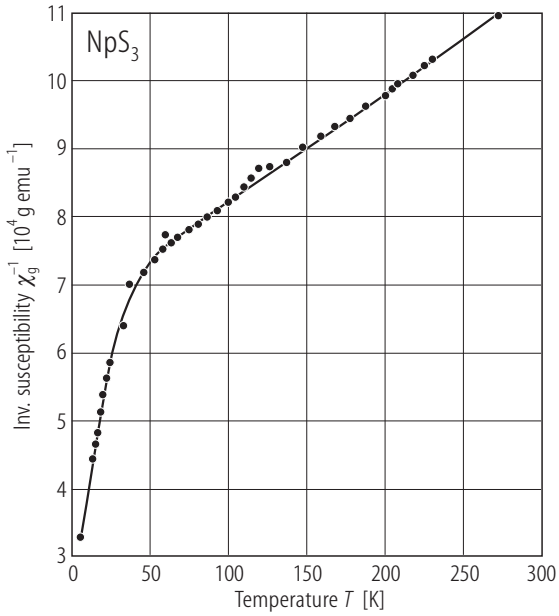

Fig. 424. NpS_3. Inverse mass magnetic susceptibility, χ_g^{-1}, vs. temperature, T [81TPGD]. The compound remains paramagnetic down to 4.2 K. The solid line is a guide for the eye. p_{eff} = 3.90(2) μ_B suggests a $5f^3$ configuration (Np^{4+}).

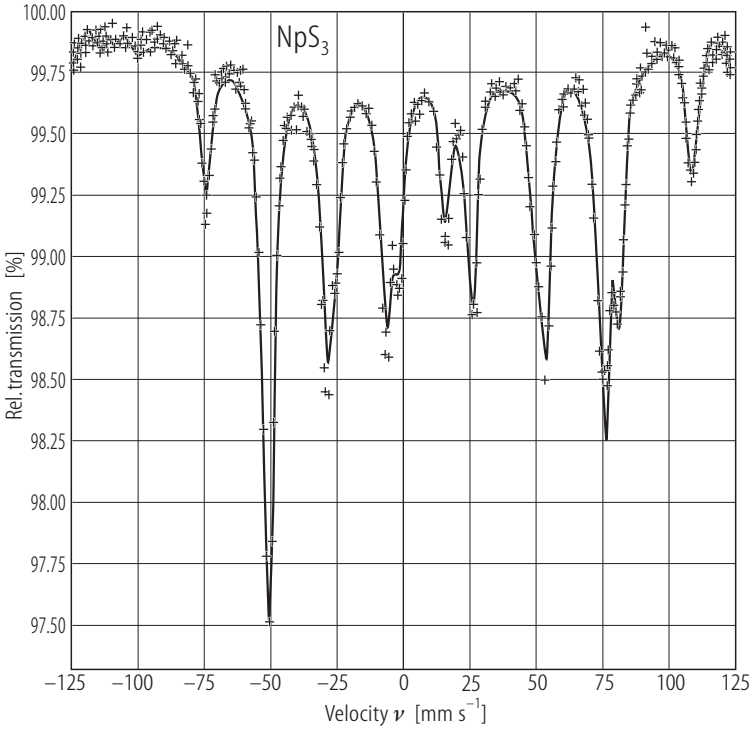

Fig. 425. NpS_3. ^{237}Np Mössbauer absorption spectrum taken at T = 4.2 K [84TJP]. The hyperfine parameters are presented in Table J. On the basis of the isomer shift value the tetravalent state of Np ions is concluded.

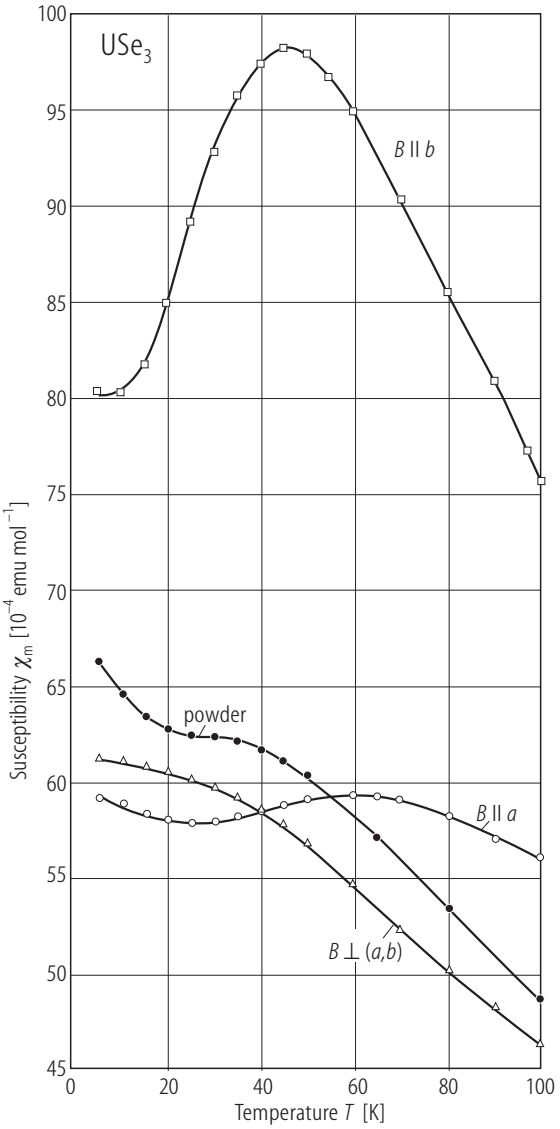

Fig. 426. USe_3, sc. Molar magnetic susceptibility, χ_m, vs. temperature, T, in the range 2…100 K, measured with magnetic field applied along the a-axis (open circles), along the b-axis (squares) and perpendicular to the (ab)-plane (triangles), as well as on a powder sample (full circles) [86N]. A large anisotropy is related to the magnetocrystalline anisotropy of the monoclinic structure. Broad maxima in $\chi_m(T)$, centered for $B \parallel a$ at 60 K and for $B \parallel b$ at 45 K, indicate a two-dimensional character of short range magnetic interactions with the magnetic moments probably aligned parallel to the chain axis b (see Fig. 416).

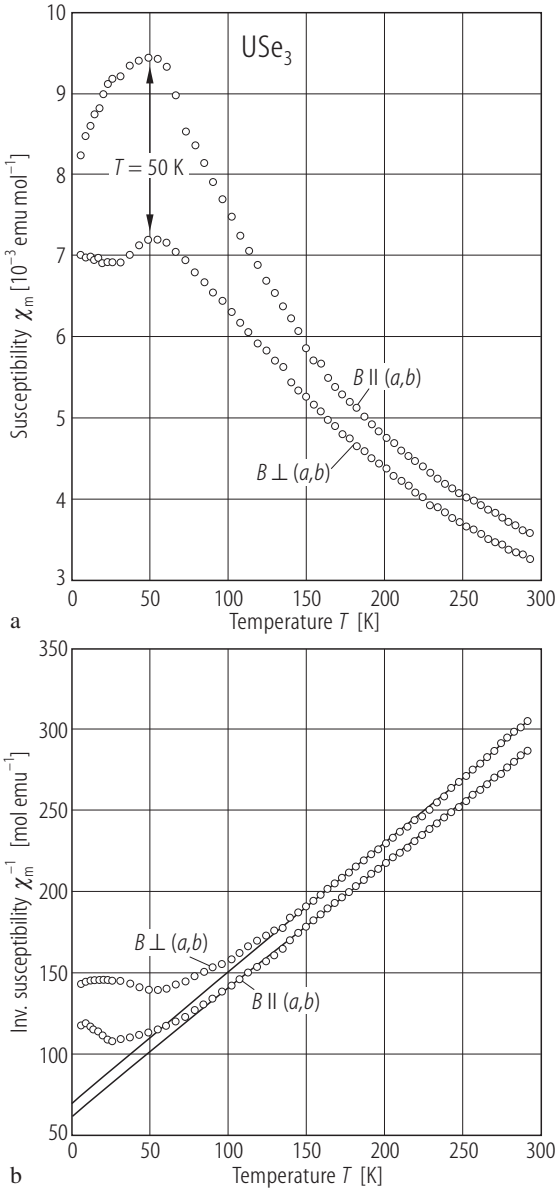

Fig. 427. USe_3, sc. **(a)** Molar magnetic susceptibility, χ_m, vs. temperature, T, measured with magnetic field applied within and perpendicular to the (ab)-plane [95S]. **(b)** Inverse molar magnetic susceptibility, χ_m^{-1}, vs. temperature, T, measured as in panel **(a)** [95S]. The solid lines denote Curie-Weiss fits with the parameters given in Table F.

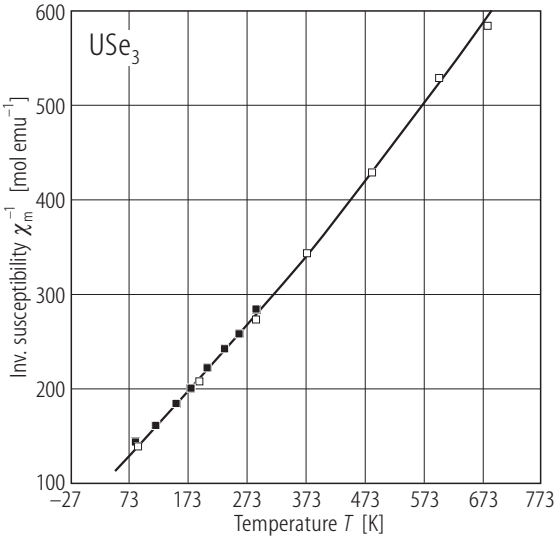

Fig. 428. USe_3. Inverse molar magnetic susceptibility, χ_m^{-1}, vs. temperature, T, in the range 80…770 K (open squares) [68GHTT]. p_{eff} = 3.05 μ_B. For comparison the data obtained by [61TS] between 80 and 300 K are shown by full squares. Note a good agreement between the results of both studies.

For Fig. 429 see next page

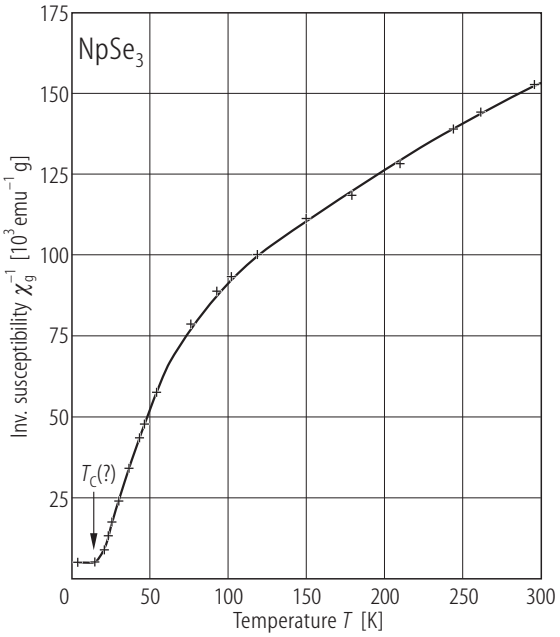

Fig. 430. $NpSe_3$. Inverse mass magnetic susceptibility, χ_g^{-1}, vs. temperature, T [76BFSW]. The appearance of ferromagnetism below 18 K is suggested. Above 110 K the susceptibility follows a modified Curie-Weiss law with the parameters given in Table F.

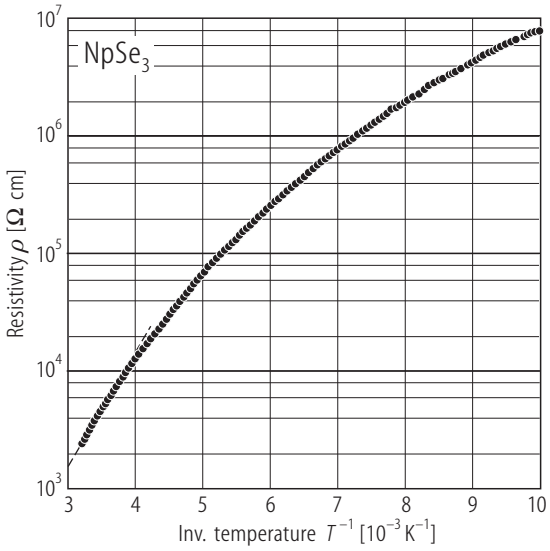

Fig. 431. $NpSe_3$. Electrical resistivity, ρ, vs. inverse temperature, $1/T$ [82BDM]. The room temperature resistivity is 3900 Ωcm. The dashed line marks an activation behaviour above 250 K with E_g = 0.37 eV. Despite that $NpSe_3$ was suggested to order ferromagnetically at 18 K (see Fig. 430) no anomaly occurs in $\rho(T)$.

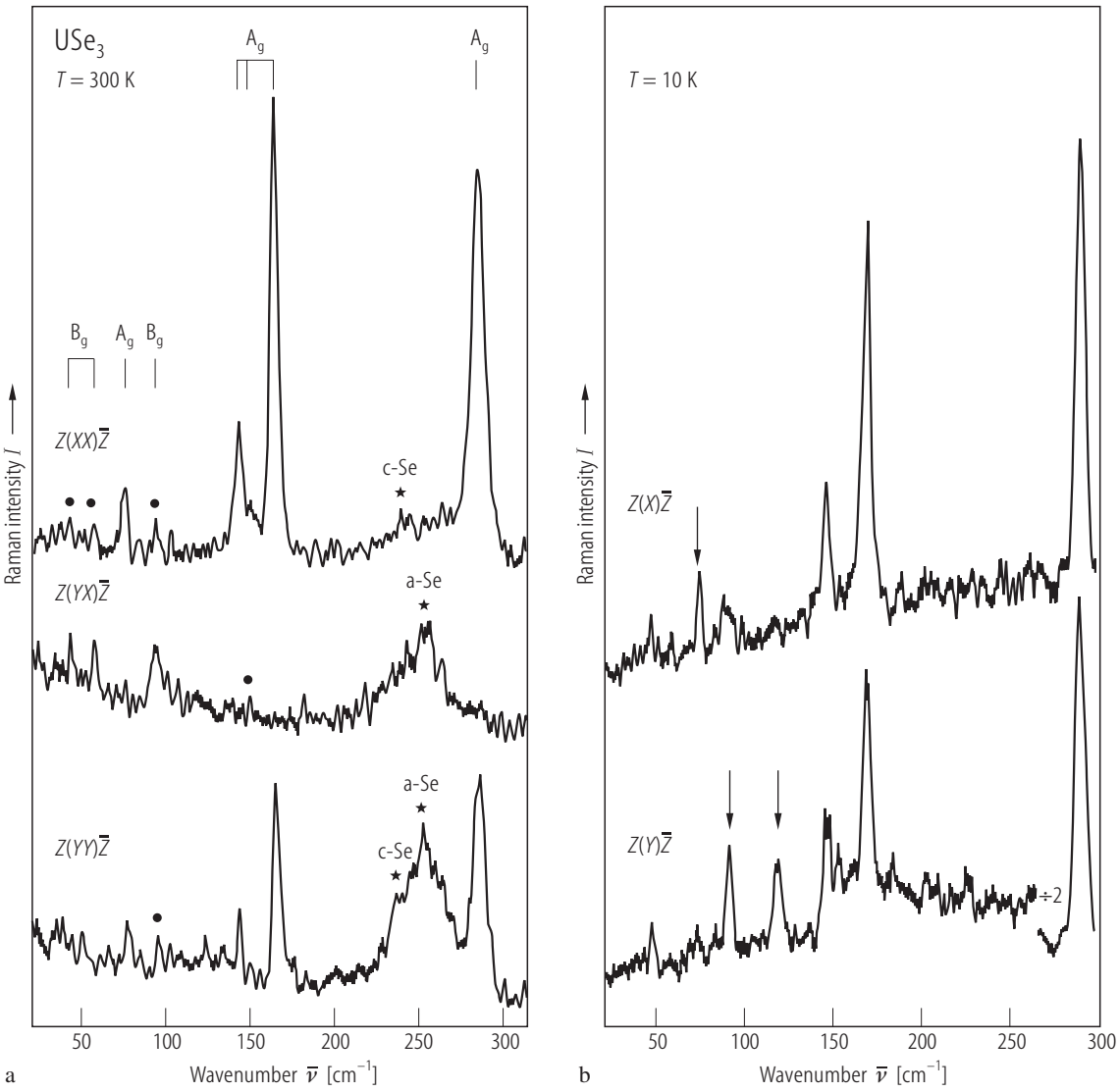

Fig. 429. USe_3, sc. Raman spectra taken at **(a)** T = 300 K and **(b)** T = 10 K, excited with the λ = 488.0 pm laser line [86NZRN,87NZRL]. The curves correspond to three different polarization configurations given by the labels $k_i(e_ie_s)k_s$, where k is the wave vector and e is the polarization of the light inside the crystal. The indices i and s refer to the incident and scattered light, respectively (for the 10 K spectra the scattered light was not analysed). The asterisks mark bands originating from amorphous (a-Se) and crystalline (c-Se) selenium. Eight Raman active phonons were observed at 300 K with the A_g (77, 144.5, 154, 165, 285 cm^{-1}) and B_g (44, 59, 96 cm^{-1}) symmetries, as given by the upper labels. The structures in the window from 96 to 165 cm^{-1} are due to internal chain deformation, the excitation at 77 cm^{-1} is an external quasi-rigid chain motion, whereas the feature at 185 cm^{-1} corresponds to diatomic Se_2. The black points indicate lines appearing in forbidden polarisations due to depolarisation effects. The arrows in the 10 K spectra mark the electronic excitations at 73, 92 and 118 cm^{-1} due to cooperative phenomena. See also Table W.

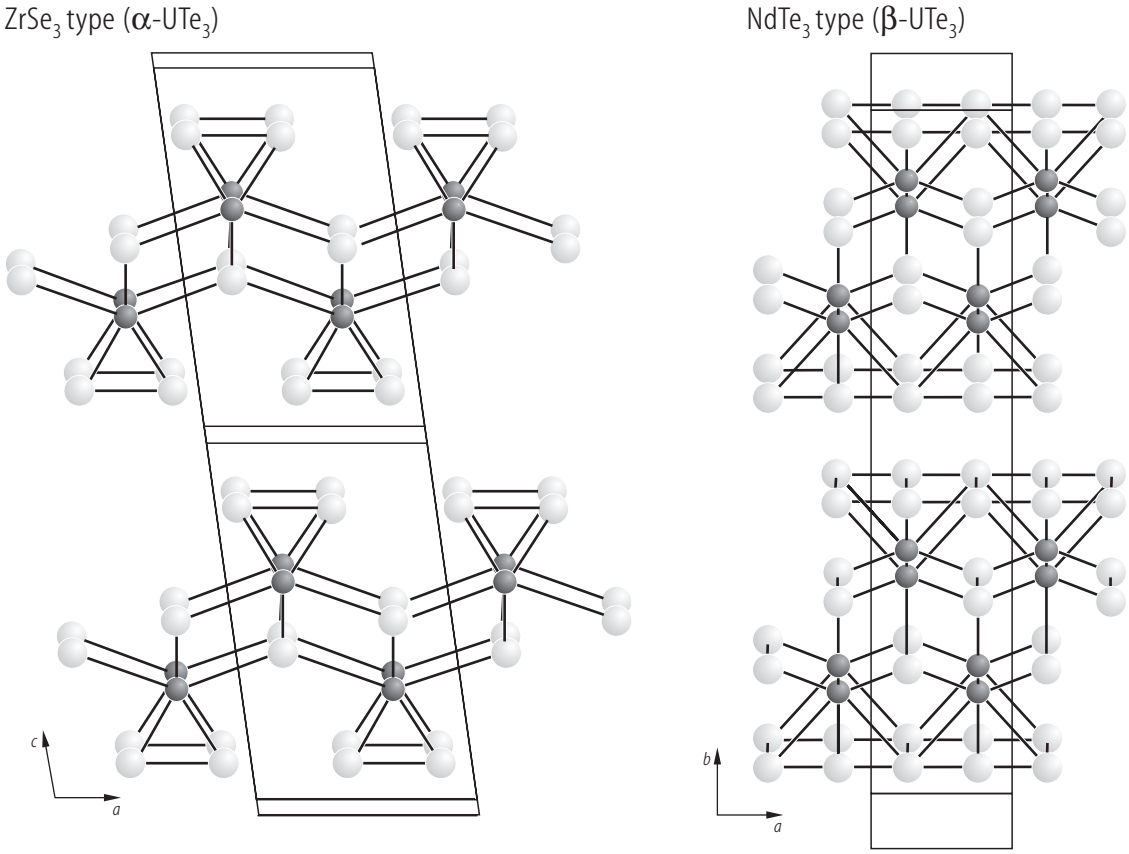

Fig. 432. α-UTe_3, β-UTe_3. Schematic representation of the crystal structures of $ZrSe_3$- and $NdTe_3$ - types showing the difference between the two atom arrangements [01PBBK]. Dark circles: U atoms; light circles: Te atoms. In monoclinic α-UTe_3 the uranium atoms are coordinated to eight Te atoms forming bicapped trigonal prismatic polyhedron. The layers of uranium atoms are separated by rows of diatomic Te_2. In orthorhombic β-UTe_3 the uranium atoms have a coordination sphere consisting of nine Te atoms in a tricapped trigonal prismatic arrangement. The tellurium atoms in layers above and below the uranium atoms plane form a square net. The difference in the atomic arrangement in these two structure types drive β-UTe_3 to be more dense.

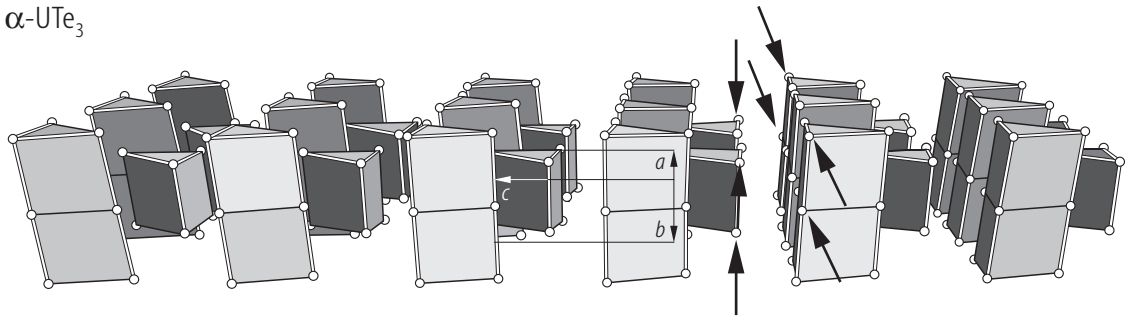

Fig. 433. α-UTe_3. Crystal structure in a [100] projection (tilted by ca. 30º) [97S2]. The arrows mark linear Te atom chains.

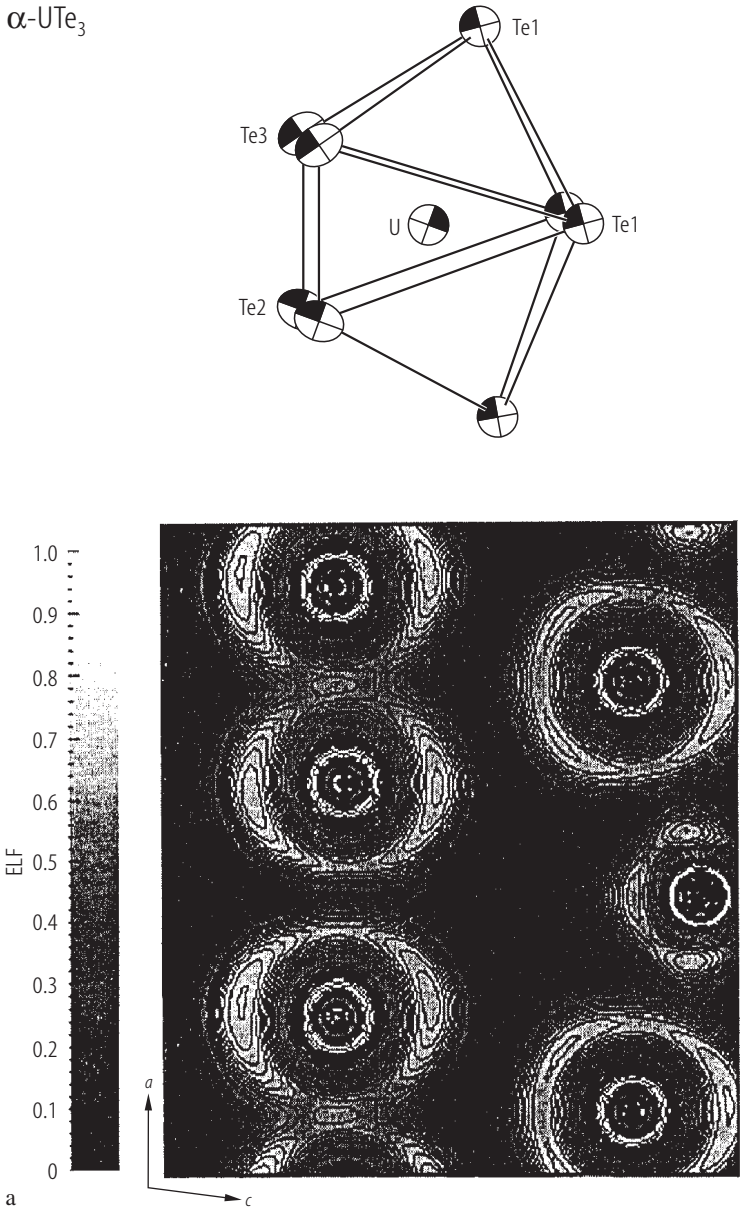

Fig. 434a. For caption see next page

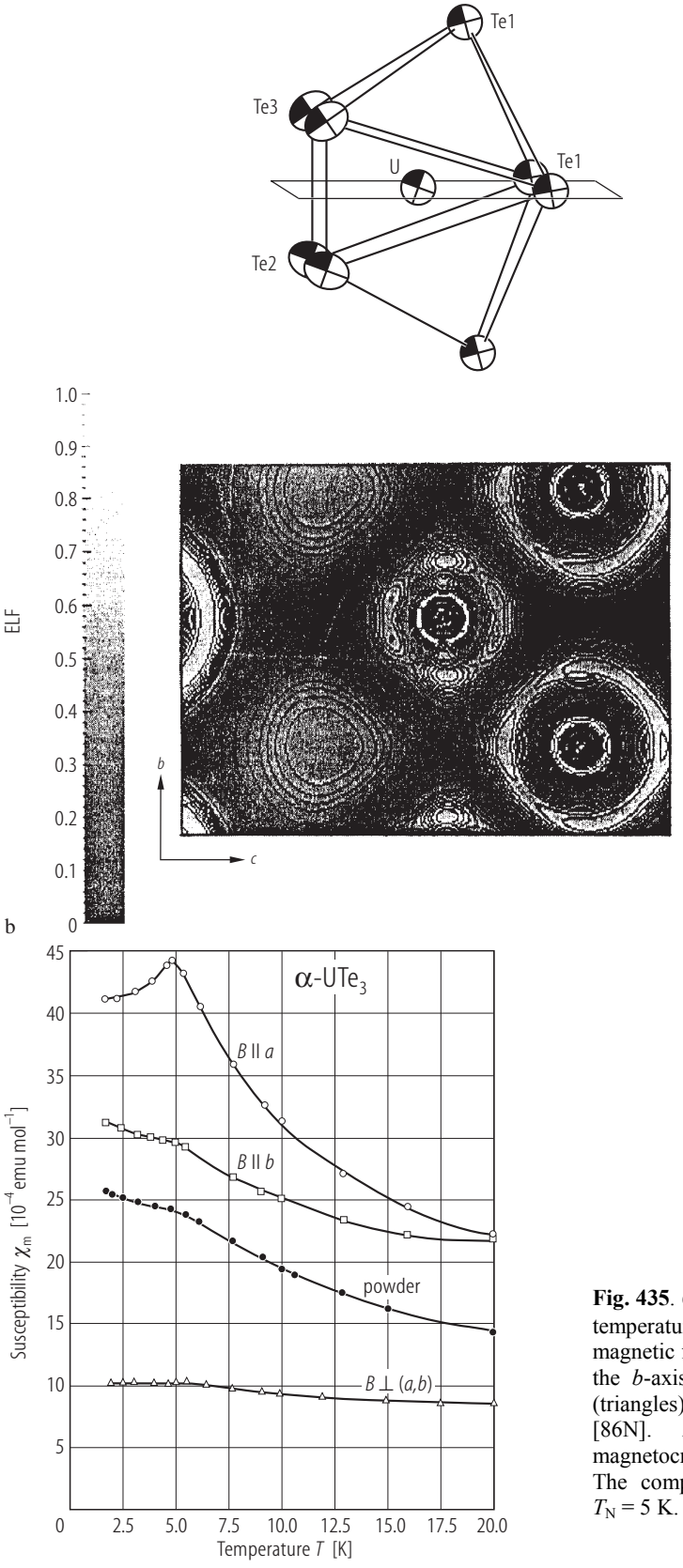

Fig. 434. α-UTe_3. Electron Localization Function (ELF) maps in the sections through the characteristic planes: **(a)** (x,1/4,~z); **(b)** perpendicular to the [100] direction at height ~0.71 [97S2]. The sections are schematically shown above the maps. For description of the topological procedure see the original paper. From the analysis of the local ELF maxima and their basins the presence of two different Te atoms has been deduced, whereby the atoms involved in the linear chains (see Fig. 433) form dumbbells. The proposed formulation with effective charges is $U^{2.0+}Te^{1.0-}(Te_2)^{1.0-}$.

Fig. 435. α-UTe_3, sc. Molar magnetic susceptibility, χ_m, vs. temperature, T, in the range 2…20 K, measured with magnetic field applied along the a-axis (open circles), along the b-axis (squares) and perpendicular to the (ab)-plane (triangles), as well as on a powder sample (full circles) [86N]. A large anisotropy is related to the magnetocrystalline anisotropy of the monoclinic structure. The compound probably orders antiferromagnetically at T_N = 5 K.

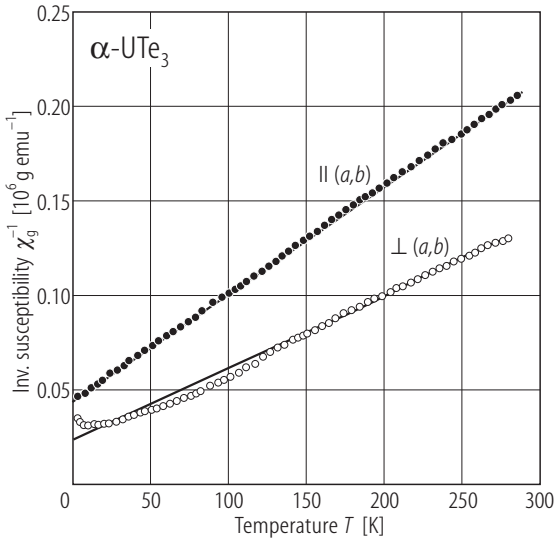

Fig. 436. α-UTe_3, sc. Inverse mass magnetic susceptibility, χ_g^{-1}, vs. temperature, T, measured on a platelet-like sample for magnetic field applied within (full circles) and perpendicular (open circles) to the (*ab*)-plane [82JSB]. The solid lines are Curie-Weiss fits of the experimental data to a Curie-Weiss law with the parameters given in Table F.

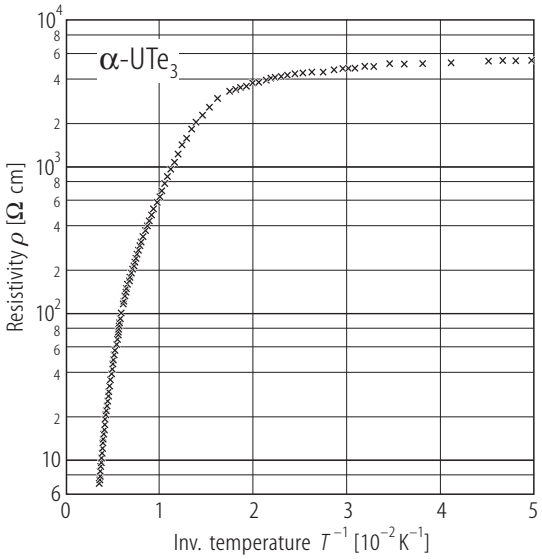

Fig. 437. α-UTe_3. Electrical resistivity, ρ, vs. inverse temperature, $1/T$, measured on pseudo single-crystalline sample [81BJS]. Note a semiconducting behaviour.

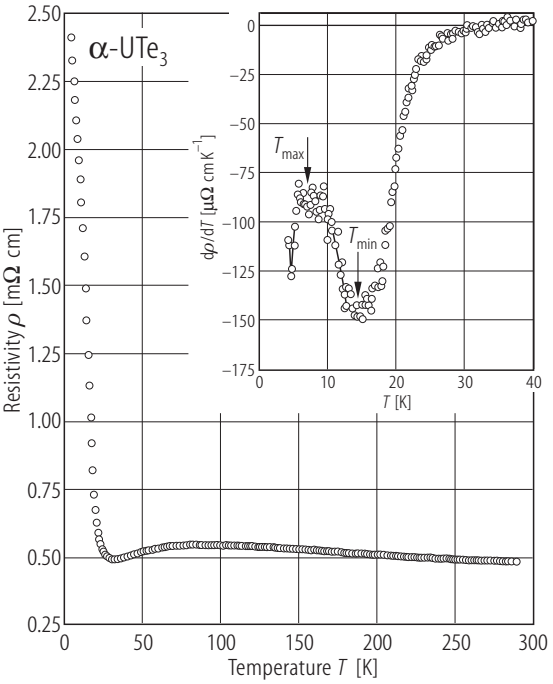

Fig. 438. α-UTe_3, sc. Electrical resistivity, ρ, vs. temperature, T, measured with the current flowing along the *a*-axis [00TKN]. Note a broad maximum centered at 80 K and a very sharp rise in $\rho(T)$ below 30 K. Inset: temperature derivative of the resistivity, $d\rho/dT$, vs. T below 40 K. The maximum at T_{max} = 5 K corresponds to the peak in $\chi_a(T)$ occurring at the same temperature (see Fig. 435).

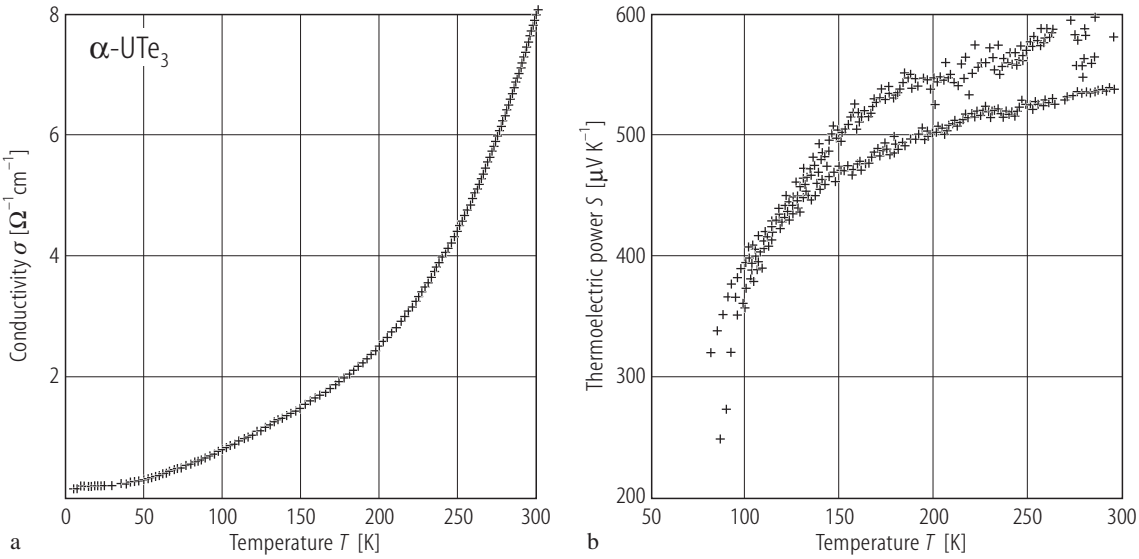

Fig. 439. α-UTe_3. **(a)** Electrical conductivity, σ, vs. temperature, T, measured on room-temperature pressed pellet [01PBBK]. **(b)** Thermopower, S, vs. temperature, T in the range 80…300 K, measured on two different room-temperature pressed pellets [01PBBK]. The compound is a p-type narrow-gap semiconductor with a large value of thermopower at room temperature S(300K) = 550 μV/K.

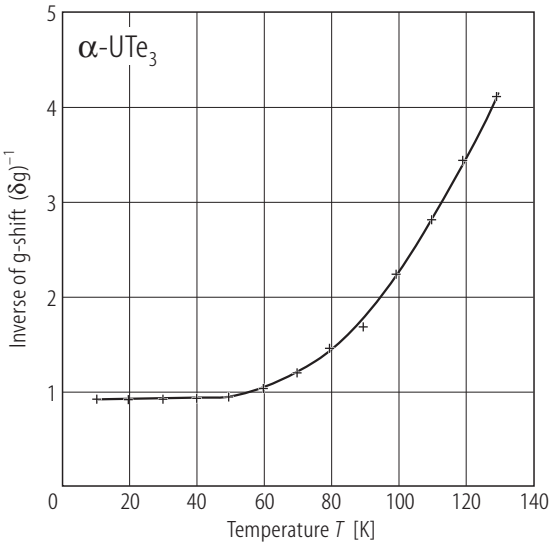

Fig. 440. α-UTe_3, sc. Inverse g-shift of the EPR line, δg^{-1}, vs. temperature, T, in the range 10…130 K [83BSJS]. The solid line is a fit to the formula $\delta g^{-1} = A + B\coth\left(\Delta / 2k_B T\right)$ derived within two-level approximation, where Δ is the energy distance between the first excited level and the ground state (Δ/k_B = 360±40 K).

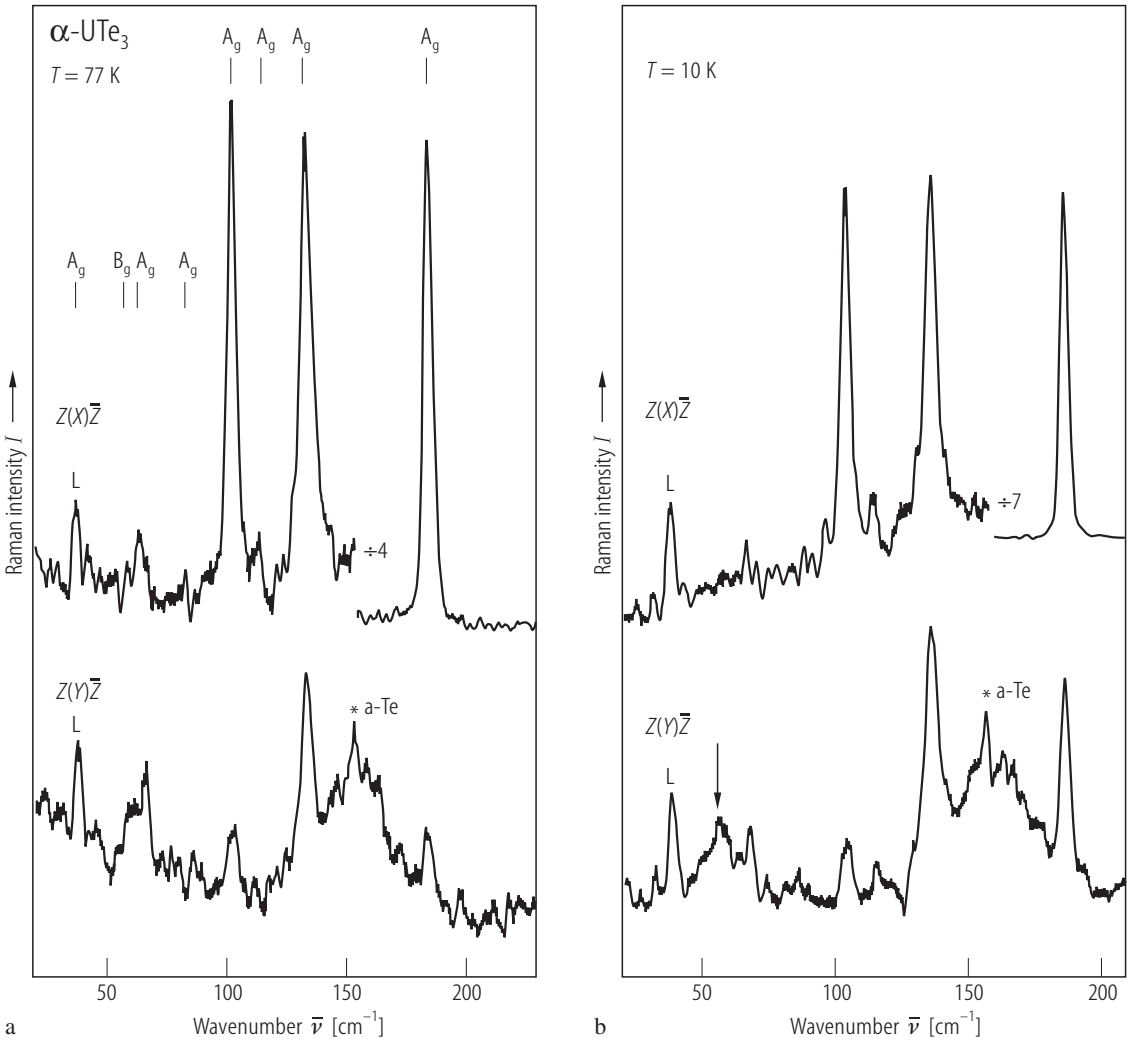

Fig. 441. α-UTe_3, sc. Raman spectra taken at **(a)** T = 77 K and **(b)** T = 10 K, excited with the λ = 488.0 pm laser line [86NZRN, 87NZRL]. The curves correspond to three different polarization configurations given by the labels $k_i(e_i)k_s$, where k is the wave vector and e is the polarization of the light inside the crystal. The indices i and s refer to the incident and scattered light, respectively (the scattered light was not analysed). The asterisk marks bands originating from amorphous (a-Te) tellurium. The label L denotes a spurious laser emission line. Eight Raman active phonons were observed at 77 K with the A_g (41, 67.5, 83.5, 102, 113, 133, 183.5 cm^{-1}) and B_g (62 cm^{-1}) symmetries, as given by the upper labels. The structures in the window from 102 to 33 cm^{-1} are due to internal chain deformation, the excitation at 183.5 cm^{-1} corresponds to diatomic Te_2. The arrow in panel **(b)** marks the electronic excitation in the band centered at 57 cm^{-1}, which has a *YY* polarization and Γ_1 symmetry. See also Table W.

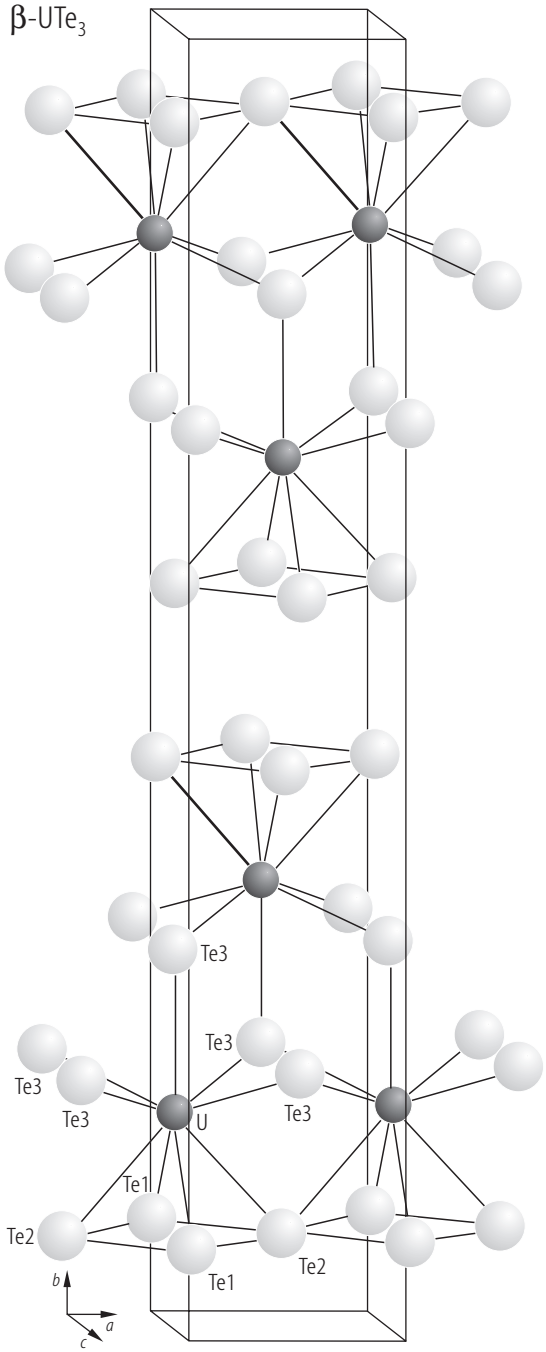

←

Fig. 442. β-UTe_3. Orthorhombic crystal structure (space group Cmcm) [89NL]. The phase was proved by [97S1] to be a nonstoichiometric compound $U_{0.9}Te_3$ with defects on the uranium sites, distributed statistically in the $NdTe_3$-type unit cell. The tellurium atoms with planar Te-4Te bonds for (010) layers are separated by van der Waals gaps, giving a bidimensional character of the structure. The uranium atoms are tetravalent, unlike rare-earth and transuranium atoms in isostructural compounds.

For Figs. 443 and 444 see next page

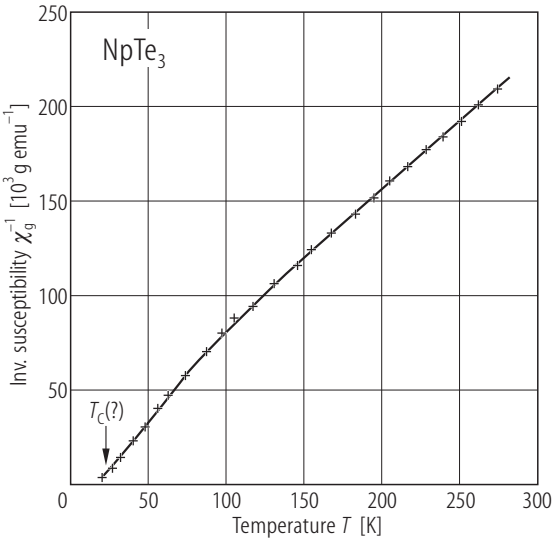

Fig. 445. $NpTe_3$. Inverse mass magnetic susceptibility, χ_g^{-1}, vs. temperature, T, in the range 25…280 K [76BFSW]. Above 80 K the experimental data follow a modified Curie-Weiss law with the parameters given in Table F. A ferromagnetic behaviour is suggested below $T_C \approx 25$ K.

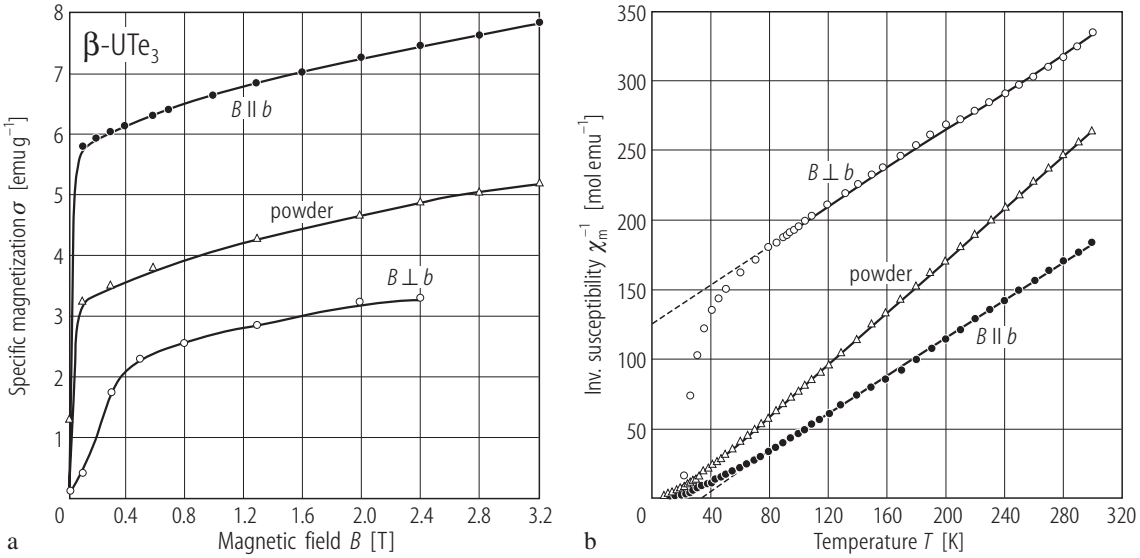

Fig. 443. β-UTe_3, sc. **(a)** Specific magnetization, σ, vs. magnetic field, B, taken at T = 2.5 K with $B \perp b$-axis (open circles) and $B \parallel b$-axis (full circles) and on powder (triangles) [89NL]. The compound orders ferromagnetically at T_C = 12 K with the magnetic moment components p_s ($B \parallel b$) = 0.63 μ_B and p_s ($B \perp b$) = 0.22 μ_B (as derived by extrapolation of the experimental data to zero field). **(b)** Inverse molar magnetic susceptibility, χ_m^{-1}, vs. temperature, T, measured as in panel **(a)** [89NL]. The lines are Curie-Weiss fits with the parameters given in Table F.

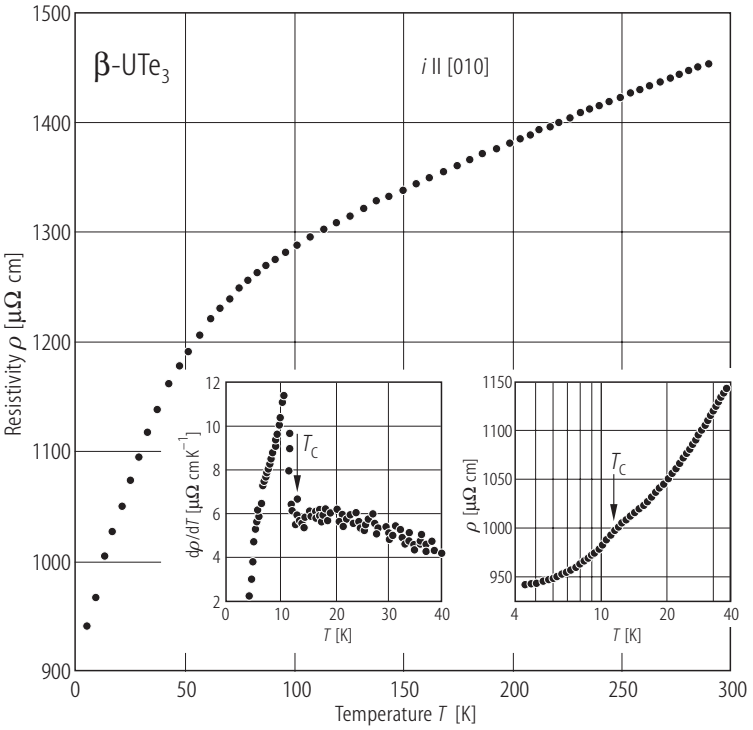

Fig. 444. β-UTe_3, sc. Electrical resistivity, ρ, vs. temperature, T, measured with the current flowing along the b-axis [00TKN]. Insets: resistivity, ρ, and temperature derivative of the resistivity, $d\rho/dT$, vs. T below 40 K. The ferromagnetic phase transition at T_C = 12 K (see Fig. 443) clearly manifests itself in both characteristics.

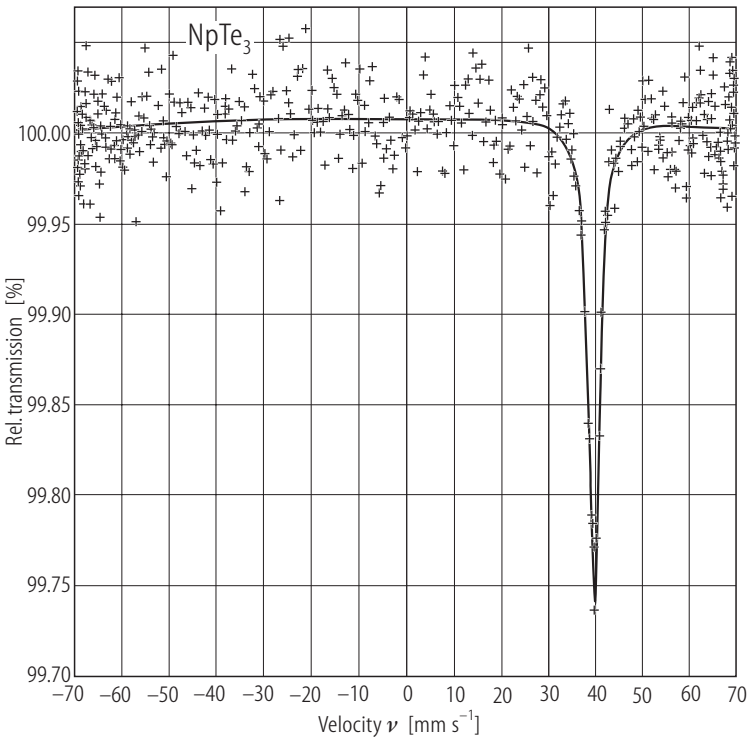

Fig. 446. $NpTe_3$. ^{237}Np Mössbauer absorption spectrum taken at T = 77 K [84TJP]. The hyperfine parameters are presented in Table J. On the basis of the isomer shift value the trivalent state of Np ions is concluded.

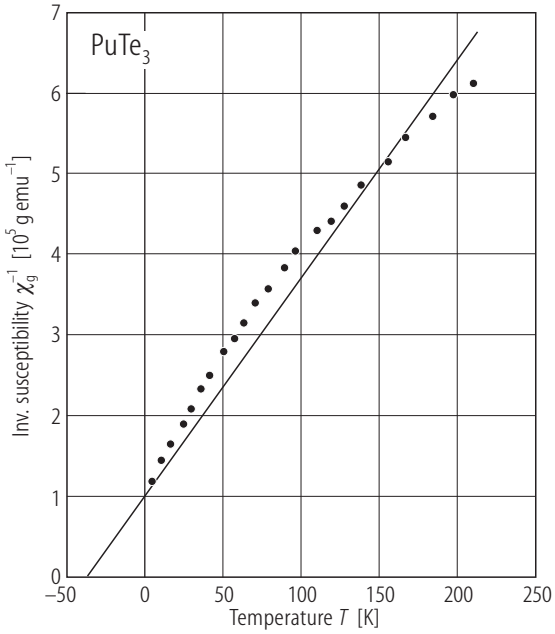

Fig. 447. $PuTe_3$. Inverse mass magnetic susceptibility, χ_g^{-1}, vs. temperature, T, in the range 5…215 K [76BFSW]. The solid line marks a Curie-Weiss behaviour with p_{eff} = 1.23 μ_B, corresponding to a Pu^{3+} ion, and Θ = –30 K.

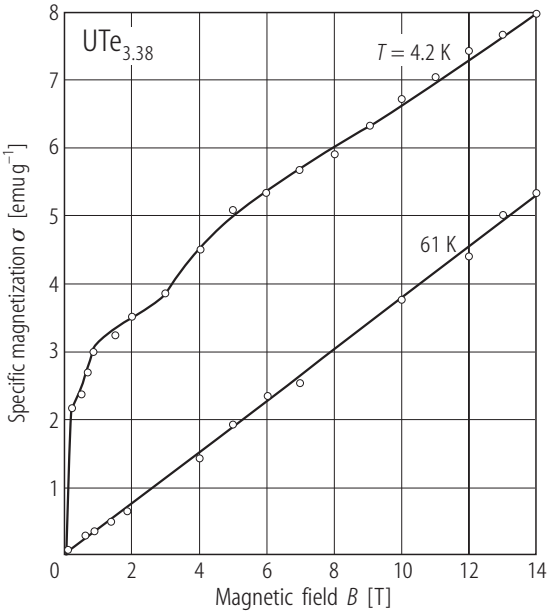

Fig. 448. $UTe_{3.38}$. Specific magnetization, σ, vs. magnetic field, B, up to 14 T, taken at 4.2 and 61 K [76S]. The magnetization value at 4.2 K and 3 T is more than three times larger than that for UTe_5 (compare Fig. 451a).

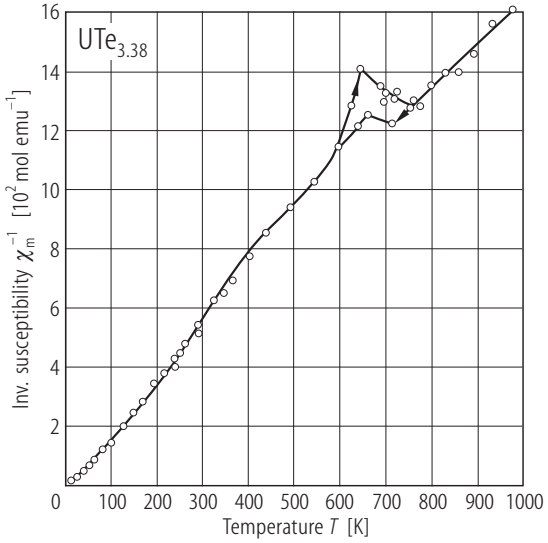

Fig. 449. $UTe_{3.38}$. Inverse molar magnetic susceptibility, χ_m^{-1}, vs. temperature, T, in the range 5…1100 K [76S]. Note an anomaly at 600…700 K with distinct hysteresis of unknown origin. The susceptibility is more than two times smaller than the respective values for UTe_3.

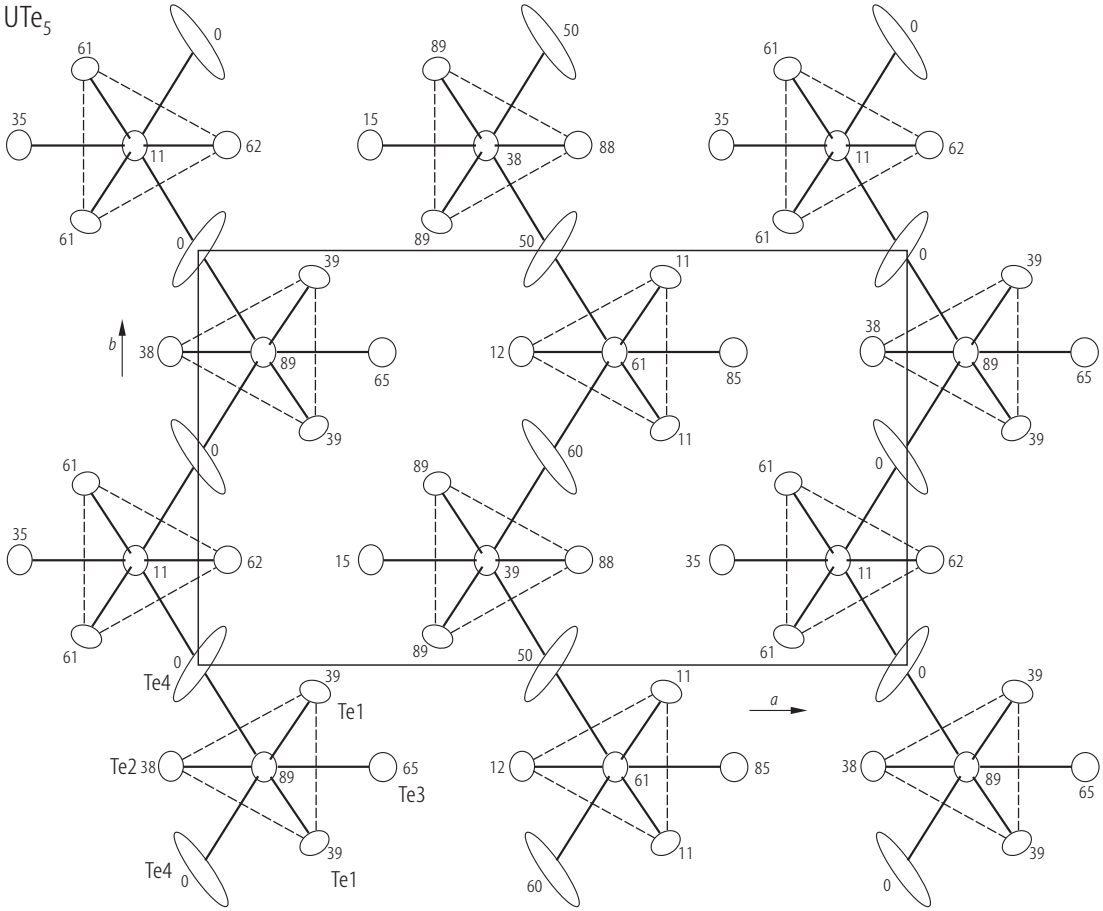

Fig. 450. UTe_5. Orthorhombic crystal structure (space group Pnma or $Pn2_1a$) projected on the (*ab*)-plane [85N1]. The numbers are the *z*-coordinates (× 10^2) of each atom, represented by a thermal ellipsoid. The uranium atoms are placed in the center of a prism built out by Te atoms which form infinite chains along the *c*-direction, sharing the triangular faces Te1-Te1-Te2 with adjacent prisms. The rectangular faces of the trigonal prisms are capped by two Te4 and one Te3 atoms (which are not in median plane) forming nine atoms coordination sphere.

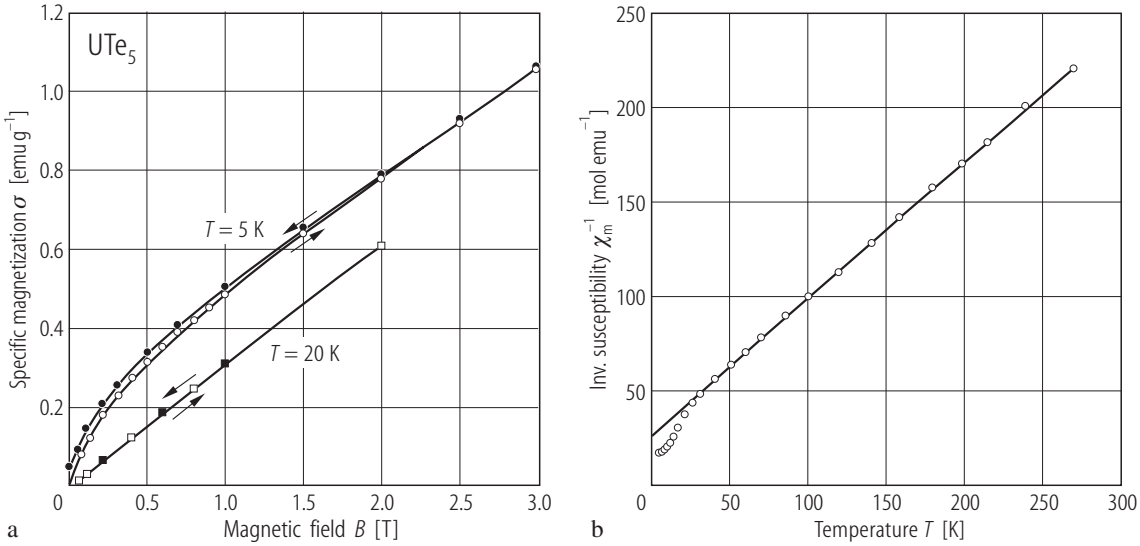

Fig. 451. UTe_5. **(a)** Specific magnetization, σ, vs. magnetic field, B, taken at T = 5 K (circles) and 20 K (squares) with increasing (open symbols) and decreasing (full symbols) magnetic field [84N2]. The compound exhibits a weak ferromagnetism below T_C = 8 K (note a weak remanent magnetization), presumably due to a slightly canted antiferromagnetic structure. **(b)** Inverse molar magnetic susceptibility, χ_m^{-1}, vs. temperature, T [84N2]. The solid line is a Curie-Weiss fit with the parameters given in Table F.

APPENDIX – PHASE DIAGRAMS

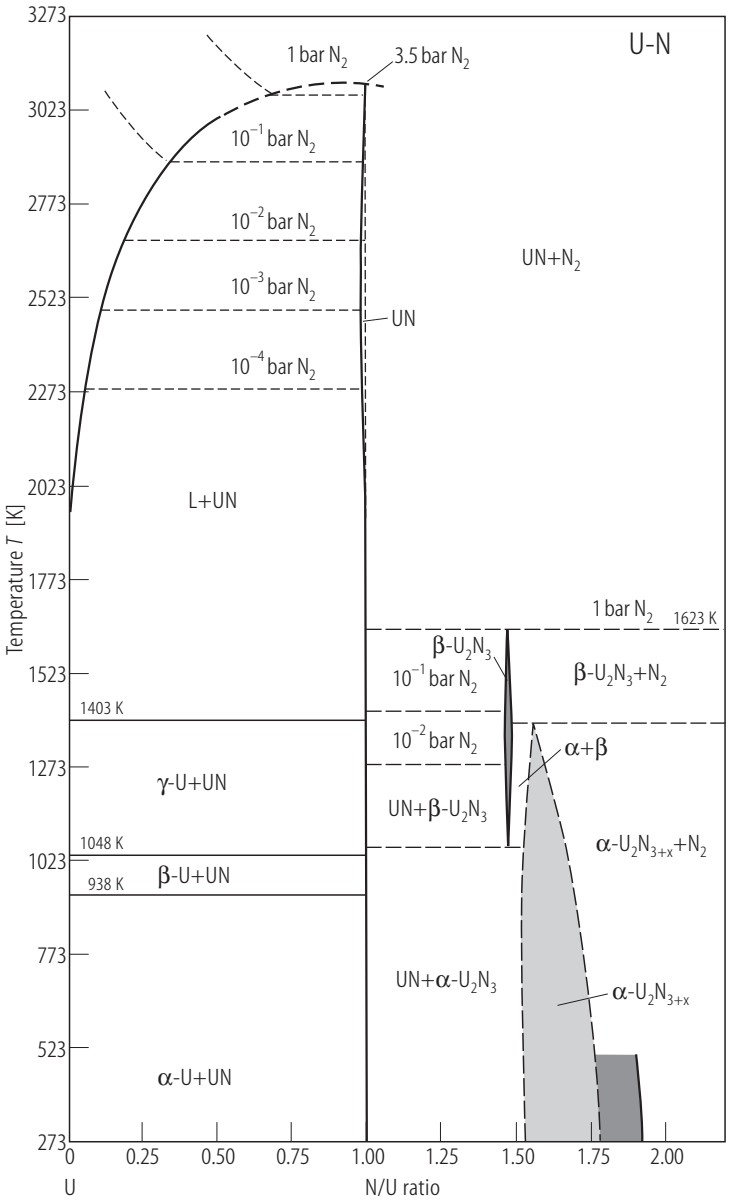

Fig. 452. U–N. Phase diagram [75H], based on that presented by [74T]. See also the diagram by [97O]. The nitrogen-poor and nitrogen-rich phase of U_2N_{3+x}, with the bcc Mn_2O_3-type structure, obtained in the reaction of uranium with nitrogen, has been established to be approximately at the atomic ratios N/U = 1.54 and 1.75, respectively (see the light-shaded area). In the studies [64TT], [73BHR] and [94MHMK] of action of ammonia (NH_3 has an extremely high nitrogen activity, a_N) on U(powder) and U(massive), respectively, the nitrides with the N/U ratio up to 1.86 (see the dark-shaded area) were reported to form via the reaction $2U + (3+x)NH_3 = U_2N_{3+x} + (9+3x/2)H_2$. See also [98NHNY] for the reaction experiments to obtain the N-rich compositions in the reaction of UC and NH_3. The hexagonal phase β-U_2N_3 is a hypostoichiometric compound around the composition $UN_{1.48}$ [66BB], which crystallizes in the hexagonal La_2O_3-type structure [62TTL]. This nitride is formed above 800 ºC in the nonpolymorphic transformation: α-U_2N_{3+x} ↔ β-U_2N_{3-y} + ½(x+y)N_2 (see [68LM] and [74T]).

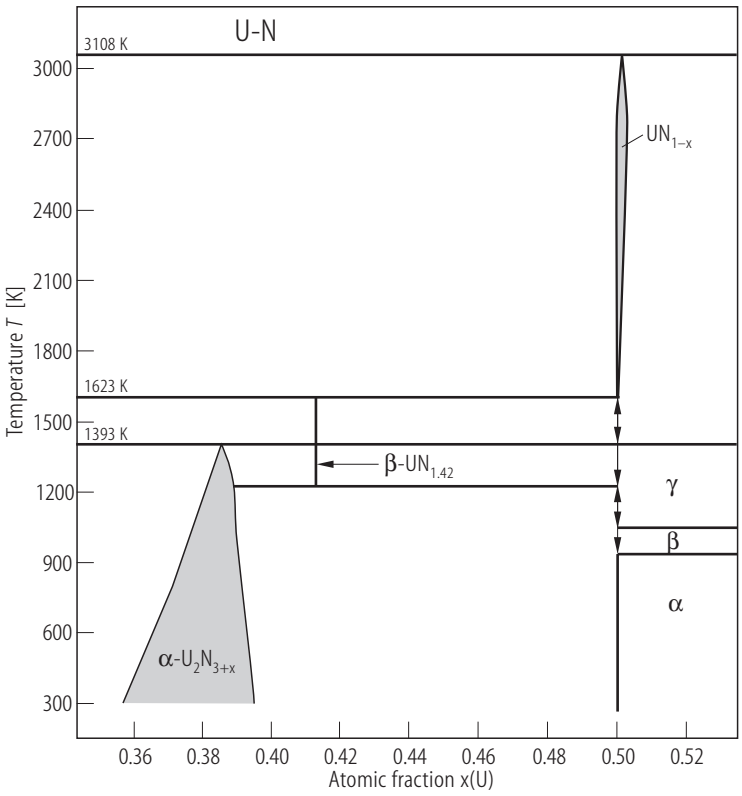

Fig. 453. U–N. Comparison of experimental equilibrium phase diagram with the calculated one [00CFC]. The thermodynamic modeling of the U-N binary system was done by critical assessment of most available experimental data provided by many researchers (experimental points are omitted). x(U) is the atomic fraction of uranium in the U-N system. The α-U_2N_3 (bcc) $\leftrightarrow$ β-U_2N_3 (hexagonal) transition temperature is 1393 K. The mean value of N content for β-U_2N_3 is 1.425 corresponding to x(U) = 0.412. The nonstoichiometry range of α-U_2N_{3+x} is $UN_{1.54–1.75}$ (0.3636 < x(U) < 0.3937). The mean value of N content for α-U_2N_{3+x} is 1.645, which corresponds to x(U) = 0.378.

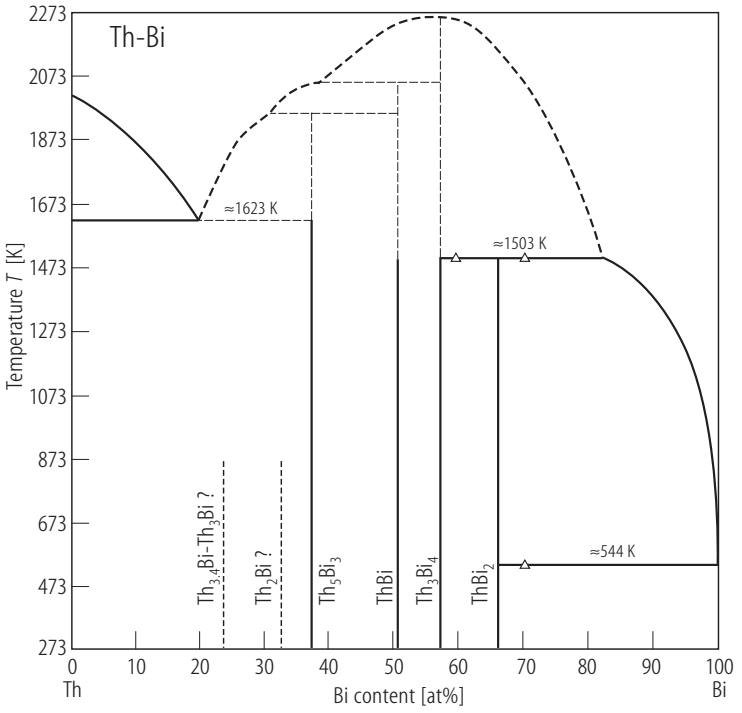

Fig. 454. Th–Bi. Phase diagram [82BBF].

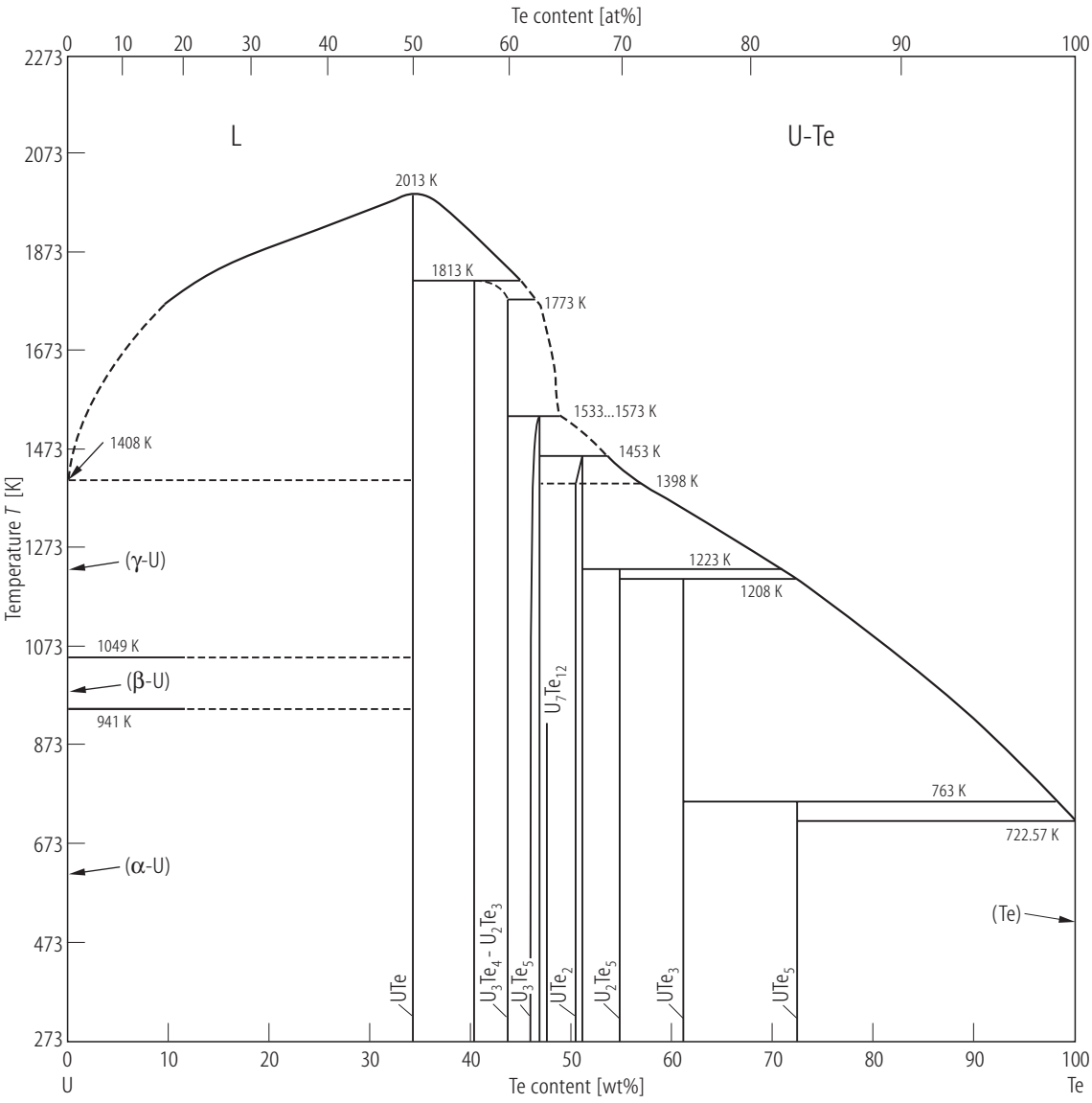

Fig. 455. U–Te. Phase diagram [91SNB].